MODIFCIATION OF THE HOT-DRY-WINDY INDEX USING HIGH RESOLUTION RAPID REFRESH MODEL DATA

by

Scott Schulze

A Thesis Submitted to the Faculty of the

DEPARTMENT OF HYDROLOGY AND ATMOSPHERIC SCIENCES

In Partial Fulfillment of the Requirements

For the Degree of

MASTER OF SCIENCE

In the Graduate College

THE UNIVERSITY OF ARIZONA

2020

THE UNIVERSITY OF ARIZONA
GRADUATE COLLEGE

As members of the Master's Committee, we certify that we have read the thesis prepared by: Scott James Schulze
titled: Modification of the Hot-Dry-Windy Index Using High Resolution Rapid Refresh Model Data

and recommend that it be accepted as fulfilling the thesis requirement for the Master's Degree.

Christopher L Castro — Date: Jan 14, 2021
Christopher L Castro

Guo-Yue Niu — Date: Jan 14, 2021
Guo-Yue Niu

Donald A Falk — Date: Jan 14, 2021
Donald A Falk

Final approval and acceptance of this thesis is contingent upon the candidate's submission of the final copies of the thesis to the Graduate College.

I hereby certify that I have read this thesis prepared under my direction and recommend that it be accepted as fulfilling the Master's requirement.

Christopher L Castro — Date: Jan 14, 2021
Christopher L Castro
Thesis Committee Chair
Hydrology and Atmospheric Sciences

Signature: Scott James Schulze
Email: sjschulze@email.arizona.edu

Acknowledgements

The Author would like to acknowledge his classmates and peers within the research group as without their support, this project would never have reached its current state. Special thanks need also be directed to Dr. Alan Srock for his assistance.

Table of contents

Abstract

Fire weather is defined as the meteorological conditions conducive to the rapid spread and intensification of a wildfire. It is generally agreed that sudden and rapid wildfire intensification is one of the greatest hazards facing wildfire managers today. The Hot-Dry-Windy (HDW) Index created by Srock et al. (2018) provides a means for predicting rapid wildfire intensification. A limitation of the HDW index is the temporal output of once every six hours when utilizing the National Centers for Environmental Prediction (NCEP) Coupled Forecast System Model Version 2 (CFsV2) data. The use of National Oceanic and Atmosphere Administration (NOAA) High Resolution Rapid Refresh (HRRR) model data has the benefits of being able to capture mesoscale processes along with a six-fold increase in the temporal outputs of the HDW index. This assists in the capture of a high fire spread rate due to a rapid change in meteorological conditions that would have been otherwise missed by the coarser resolution provided by the original model. This analysis was made with the meteorological model data in the window of a historic wildfire case featuring Santa Ana winds (SAWs). The HRRR data was found to be much more capable of modeling the terrain of the coastal mountain ranges in the southern California area. The mesoscale modeling capability also aided in the HDW Index not suffering as severely from artificially lowered values near the coast when compared with the CFsV2 output.

Introduction

Wildfires are among the costliest natural disasters in the United States. The Thomas fire used as a case study cost an estimated 2.3 billion dollars in damages including fighting and containment according to the Insurance Information Institute. Climate change in the southwestern United States is increasing this threat. The number of wildfires has been decreasing, however the severity and spread (acres burned) has increased over the past three decades (Hoover and Hanson, 2021). According to Hoerling et al. (2013), the climate is warming and drying, with the most recent decade (2001-2010) being the warmest and 4th driest in the record from 1901-2010. This change in the climate favors the pattern of larger, more severe wildfires and the variables associated with that change are measured by the HDW Index.

Fire weather is broadly defined as the conditions conducive to the spread and intensification of a wildfire. Wildfire spread is among the more difficult aspects for fire managers to cope with in a deployed situation. The HDW Index developed by Srock et al. (2018), sought to provide fire managers with a tool to provide a means of forecasting for a high fire spread rate period using only meteorological variables. This index contains only positive values that vary from region to region. This allows the HDW Index to be widely applied, however what qualifies for an extreme event is different for each

geographic location. The pioneering nature of this work and its use of a climate reforecast dataset has limited the temporal output of the index to every six hours. The need is apparent to find a means of utilizing the HDW Index to increase the temporal resolution outputs to swiftly capture changes in conditions that enhance fire spread.

The HDW Index also addresses a finding from Byram (1954) in which he states that the winds, not only at the surface, but also in the lowest section of the atmosphere, "from the tops of the trees down," is more representative of the risk of an enhanced burn event.

According to Raphael (2003), strong wind events such as SAWs in the cold season pose a significant threat for wildfires in southwestern California. While the temperature is not high, the strong winds coupled with the drying conditions of the SAWs slight temperature increase both act to enhance the risk of wildfire.

Motivation

The CFsV2 model data generate temporal outputs every six hours, and of the four model runs for any given day, only three are utilized. This is because, due to the diurnal cycle, one of the four outputs will occur during the approximate overnight hours and does not give a clear signal of the magnitude of the HDW Index. While not explored in this paper, the HRRR model has an hourly model output, enabling a more precise utilization of the model.

There exists a need for a fire weather index to utilize a higher spatial resolution than the current 0.5 x 0.5-degree grid, as the complex terrain in most locations around the globe do not allow the model to accurately account for the changes in terrain. This follows from the Santa Ana Wildfire Threat Index (SAWTI) created by Rolinski et al. (2016), which runs on a 3 x 3 km grid. These changes in terrain can produce local funneling effects given appropriate wind conditions, which can accelerate the spread rate of a wildfire in a sub-grid sized area. The need for a greater temporal resolution is necessary given wildfire's capacity for exceptionally rapid development and growth if favorable conditions are present described by the HDW index.

The reason for increasing the temporal resolution is to definitively discriminate what the ideal temporal resolution is for a given area and time of year. While this paper only addresses a single wildfire case in the southwestern United States, the hourly output could be used to identify the most effective hours of output to further increase HDW Index outputs in identifying potential high spread risk periods and have a greater temporal resolution to make identification of trends in the pattern easier.

This project is also motivated by a desire for real-world application and will support the development of a real-time operational product using the similarly-scaled Global Air-Land Weather Exploitation Model (GALWEM) data as its source. This effort is being headed by the scientists within the United States Air Force's 25th Operational Weather Squadron OWS's Science Team.

Background

The HDW Index is unique among other fire weather indexes in that it is a purely meteorological tool for assessing the risk of wildfire spread. This is an advantage for Incident Meteorologists deployed to a wildfire event, as there is a reduction in complexity by not needing fuels information to assess the risk of fire spread directly and is the only such index currently available to do so. As described by Srock et al. (2018), the HDW Index is a product of the temperature as a factor in the saturation mixing ratio (e_s) and the vapor pressure with a given specific humidity (e(q)). The vapor pressure deficit (vpd) then is the difference between the saturation mixing ratio and the mixing ratio (Equation 1). The temperature is not directly applied in the HDW calculation but is directly related to the vpd as indicated by Figure 31. The ultimate formula for the HDW index is shown in Equation 2. The winds in approximately the lowest 1,000 feet of the atmosphere are averaged (U). This term is then multiplied by the vapor pressure deficit and yields a positive number always.

Equation 1: Vapor Pressure Deficit calculation

$$VPD\ (T,q) = e_s(T) - e(q)$$

Equation 2: Calculation of the HDW Index

$$HDW = U \times VPD(T,q)$$

The HDW Index is closely related to the SAWTI. The SAWTI's relation to HDW is that it also tracks the temperature, moisture, and wind, though designed and calibrated specifically for the southwestern United States. These characteristics make it lesser reaching and more geographically specific and will be addressed below.

The SAWTI utilizes the surface wind speed and the dewpoint depression, but critically requires some knowledge of the fuels condition. This need is removed in the HDW Index by utilizing the vapor pressure deficit (vpd) at the surface. The vpd is defined as the difference between the saturation mixing ratio (e_s) and the mixing ratio (e) for a given temperature. This is an exponentially-scaled relationship and as was described by Srock et al. (2018) when the temperature is high and the mixing ratio is low for a given area, the vpd is large, leading to an overall dry condition. This represents a shift in the

conventional thinking, away from the notion that fuels must be already thoroughly dried before the risk of combustion in a wildfire would increase significantly. The idea being that a moist fuel in a high vpd environment will more readily and quickly give up its moisture to the environment, rapidly drying what would traditionally be considered a less viable fuel source. This, therefore, is how the HDW Index is accounting for the fuel conditions using only a meteorological variable. Another way in which the SAWTI and HDW Index vary is in the wind component. For the SAWTI, only the surface winds are measured as it was found to be most critical of the spread of a large fire in fine fuel sources. By comparison, the HDW Index samples the lowest levels of the model, providing a wind profile, which can help identify a more robust wind event which would be more capable of spreading fire via firebrand more so than a strong surface wind alone.

While there are no specific definitions for a SAW event, there are several rules of thumb. For the purposes of this paper, we will use the guidance put forth by Small (1995) in which a SAW is identified by at least a 10 hPa difference in MSLP between Los Angeles, CA and Tonopah, NV. This fire event was also strongly influenced by a finding noted by Raphael (2003), in that the average duration of a Santa Ana wind event is 1.5 days. In the case presented, the wind event was 30 hours, during which nearly 60,000 acres burned. This was more than any other day in the life of the fire except for the day of ignition. A wildfire spreading via SAW events are also in congruence with a feature noted by Byram (1954) in that they are manifested as a mesoscale feature within a stably stratified atmosphere (Abatzoglou et al. 2013).

Meteorological Analysis

For the purposes of this paper, the traditional "top-down" approach will be used and the analysis will begin at the 850 hPa level. The 850 hPa, 925 hPa, and surface charts will be analyzed. As needed to highlight an important feature, the observations in Appendices IA-C will also be referenced for the reader. Due to the strong diurnally influenced nature of both the patterns driving SAW events and the minimization of HDW values overnight, the 0600 UTC charts will not be analyzed. This case was chosen for its relatively benign upper air conditions, with a large-scale ridge in place over the western United States.

Important features within this ridge include the statement put forth by Brewer et al. (2012): warming in the lee side region terrain barriers creating adiabatic warming and offshore flow acting as a focal point for, in this instance, mesoscale cyclogenesis. Another feature that was discussed by Brewer et al. (2012) is the large-scale inverted trough feature. These inverted troughs climatologically form during the cool season and at a maximum intensity can establish a pronounced area of low from the southern border of the United States to the Canadian border. This feature has generally low pressure along the coastal areas buffered by a large area of high pressure over the

Great Basin region, a natural formation location, with a large plateau at a high elevation. This feature creates a large pool of very cold high pressure air. The coast experiences lower pressure from the temperature modulating Pacific Ocean. The cool currents present on the western coast of the United States are a secondary reason for the formation of this pattern in the cold season, as in the other times of year, the land of the California coast is too warm to cause the water to generate the necessary depression in surface pressure.

Starting with the 850 hPa analysis for 1200 UTC on the 9th of December (Figure 2), the synoptic ridge is visible. Additionally, there is a weak signal of the mesoscale low-pressure area centered over the coast immediately over the area of interest. At the center of this mesoscale low, the wind should be nearly calm. This is supported by the Oxnard CA METAR observation shown in appendix IA from 1028 UTC where the winds were reported as being 3 knots, just above the calm threshold. It is also noted that there is both a temperature and pressure gradient between Tonopah, NV and Los Angeles, CA, paralleling the Sierra-Nevada Mountains. All of these features indicate a potential for a southwest to northeasterly oriented wind but are also too weak at this time to generate a SAW condition. Moving to the 925 hPa analysis for the same time as shown in Figure 3, the pressure gradient is relaxed and the strong temperature gradient along the California-Nevada border is also relaxed slightly. The high-pressure area over the great basin region is also stretched meridionally from northwest to southeast. This feature is important as noted by Rolinski et al. (2016) as being one of the potential signals for a cold season Santa Ana wind (SAW) event. At the surface, Figure 4, there is a strong pressure gradient to the northeast of the Los Angeles. There is also evidence to support a land breeze the air temperature on the surface at Los Angeles is 6°C while the ocean surface water temperature found in appendix 2, is 15.5°C this higher temperature over the ocean creates a weak area of lower pressure as seen in Figure 4. Moving on to the 850 hPa analysis for 0000 UTC on December 10th, the pattern looks similar to what was analyzed for the 1200 UTC analysis. Features of note at this time are the broadening of the high pressure located over the great basin and the relaxation of both the temperature and pressure gradients.

Moving down to the 925 hPa analysis (Figure 3), there is evidence of a weak inverted trough which is complemented by the land breeze shown in the observation at Los Angeles, with a five-knot wind moving offshore to the relatively warmer ocean air. This weak inverted trough, while much weaker than studied by Brewer et al. (2012), is nevertheless a signal of a tightening pressure gradient and would influence increasing winds. The temperature is 19°C at this level. Again, the cooler air over the great basin region remains, with a large temperature gradient over Nevada, Utah, and southern Idaho as was noted in the 850 hPa analysis.

The surface analysis for 1200 UTC (Figure 4) contains an interesting observation of calm winds and a surface temperature of 6°C at Los Angeles. Coupled with the analysis from the levels above, indicates the presence of an inversion. This was noticed by Byram (1954) as being a good environment for the growth and spread of wildfire. The observation of smoke both on the surface analysis and within the METAR observations for Oxnard, CA and Los Angeles, CA (Appendices IA and IC respectively) supports this as well, with the fire already burning, the smoke is trapped within the confining layer. Historically, this caused record levels of air pollution within the Los Angeles area. This inversion is illustrative of the integrity of the HDW Index analysis. Other fire weather indices such as the SAWTI only considers the winds at the surface while the HDW Index measures approximately the lowest 1,000 feet of the atmosphere.

The local METAR for the nearest airport, Oxnard, CA (Found in Appendix IA) was not indicating any of the traditional threats such as wind, with the 1200 UTC observation were still only six knots. The winds would accelerate rapidly in the following few hours, first meeting the criteria proposed by Small (1995) at the 1700 UTC observation, with a station pressure difference of 0.34 inches of mercury or 11.51 hPa. This marks the beginning of the SAW conditions that would last for approximately the next 30 hours which is in general agreement with findings from Raphael (2003), which noted that SAW events were on average 1.5 days in duration.

For the 1800 UTC surface analysis on December 9th (Figure 5), the area of high pressure has further strengthened and expanded to well north of the United States-Canadian border. The pressure gradient at the surface has increased from the 1200 UTC analysis. It bears repeating that the orientation of this pressure gradient is important, as it parallels the coastal ranges in the Los Angeles basin and creates a perpendicular wind. Looking at the METARs, the 1800 UTC observation saw the pressure difference between Tonopah, NV and Los Angeles has remained constant from the previous hour, however the temperature saw a rise of 2°C and the dewpoint dropped by 2°C. Indicating that the dry SAW has fully set in and that the rise in temperature is not simply daytime heating.

The 0000 UTC 850 hPa analysis for December 10th (Figure 6) shows that the high pressure over the great basin region as weakened slightly. This weakening however has a positive effect for the SAW conditions by concentrating the high pressure more centrally over the Great Basin region, very near the shared border between Idaho, Nevada and Utah. This positioning more favorably establishes the orientation of the gradient between Tonopah, NV and Los Angeles, CA to better align with the orientation of the mountains within the coastal range.

Descending to the 925 hPa analysis for the same day (Figure 7) it is quickly seen that there is a weak north easterly wind. Also visible are the warmest temperatures in the eastern Pacific region with a closed temperature contour above 22°C just offshore from

the location of the wildfire area. The pressure gradient is also parallel to the coast, in agreement with the analysis above. Moving down to the surface analysis for this time (Figure 8), a small section of the trough from the 1200 UTC analysis is seen inland over the area of the wildfire. Analysis of the METARs from Oxnard, CA at this time shows a dewpoint of -13°C which is a depression of 12°. This drop in moisture occurred in a scant nine hours. This is a dry air is being driven by the observed wind of 15 knots. The winds at this time have receded from the maximum values of 20 knots gusting to 30 knots three hours previously. The pressure difference between Tonopah, NV and Los Angeles is 11.85 hPa, still meeting the SAW criteria discussed previously. Interestingly, this is the same difference that gave rise to the maximum wind values three hours previous. This indicates that there is another feature of the SAW that is creating the increased or decreased winds at this time. From the standpoint of atmospheric dynamics, due to the temperature gradient noted above, there would a be an ageostrophic wind which could add to the velocities beyond what the pressure gradient alone could produce.

At the surface at 0600 UTC (Figure 9), the analyst added an inverted trough notation for the first time. Additionally, a very localized pinching of the pressure gradient in the mountains directly northeast of the wildfire burn area in the Topatopa Mountains which are a part of the Transverse range. Despite this being overnight, the winds continue to be strong with winds sustained at 14 knots and gusting to 17 knots.

In the morning at 1200 UTC at 850 hPa (Figure 10), the high pressure system has strengthened further overnight with heights increasing by at least 30 decameters. From the previous analysis, the high has also elongated and shifted slightly south, more along the Nevada-Utah border. The evidence of the inverted trough also has a weak signal at this level with a distinct northerly crease in the isobars just offshore.

Shifting down to the 925 hPa analysis (Figure 11) for the same time, the area of high pressure has expanded and shifted south, and there is an enhanced pressure gradient across the southern section of California, particularly along the California-Nevada border. This is very similar to the nature of the surface analysis (Figure 12), the biggest change from the previous timestep is there are now three isobars over the area where previously there had only been two pinching together. This is contradictory to information supplied by the METAR from Oxnard (Appendix IA), with winds of only 8 knots. Consistent with the previous chart, the inverted trough is also drawn on the surface analysis. All of this is preparing for generating the winds which would lead to a colossal burn day in the fire.

Because of the publishing schedule, there are no analyses except for the surface analysis at 1800 UTC. On the 1800 UTC surface analysis (Figure 13), the inverted trough is stronger and more pronounced than it had been; however, it was dropped from the analysis. The pressure gradient has relaxed slightly, but oriented to be more parallel

to the mountain ranges. The temperature gradient however has increased sharply with a surface temperature of 79°F at Oxnard, CA and 36°F in Tonopah, Nevada, generating a temperature gradient 43° over approximately 294 miles.

The turn of the day, 0000 UTC of the 11th marks the end of the SAW conditions. For the 850 hPa analysis (Figure 14), the high pressure system maintains its strength and moves farther to the south and west. This takes the high pressure out of the ideal position for a SAW. Moving down to the 925 hPa analysis (Figure 15), it is first noticed that the inverted trough has dissipated completely and the pressure gradient across southern California has relaxed considerably. There is also a weak southerly wind depicted in contrast to the persistent east-northeasterly flow that had been present for the previous 30 hours. Finally, at the surface, the pressure gradient has weakened and shifted, reducing the effect of channeling through the mountains. This is reflected with the METAR observation at Oxnard, CA with only an 11 knot wind. At this time the pressure difference between Tonopah, NV and Los Angeles, CA is 12 hPa, but again, shifted due to the loss of the inverted trough to the west, disabling the wind from moving through the mountain passes. Moving forward in time from this observation, the pressure steadily rises, reducing the pressure gradient necessary to maintain the SAW criteria.

Methods

To convert from the CFsV2 data to HRRR data, the greatest change required was to adjust from relative humidity which is what is used by the CFsV2 model to specific humidity found in the HRRR model data. Following this adaptation, a pressure conversion calculation needed to be made as the outputs were found to be low by a factor of 10. Once those two adjustments had been made, an output file was created to store the calculated values for later processing into the images found below.

A historical wildfire case was selected that featured a rapid spread as the result of Santa Ana winds. For the purpose of this project, the case chosen was the Thomas fire of southern California in December of 2017 (Figure. 1), focusing on December 9th, 10th, and 11th for this study. December 9th represented a low fire spread day for the fire, while December 10th represented the second largest spread day of the entire wildfire event, leading to decreased spread again on the 11th.

This case was chosen to limit atmospheric changes due to moisture and temperature, such as in a frontal passage during which winds may rapidly intensify. However, there is commonly a pronounced moisture gradient associated with a front as well, making it difficult to isolate any specific variable with which the HDW Index is concerned. Choosing southern California at this time of year also reduces the effects of abnormally

high temperatures that may be found in a desert southwest case, since, according to Abatzoglou et al. (2013), Santa Ana winds are generally a cold season phenomenon. A Santa Ana wind case was chosen since there is little moisture associated with these wind events given their leeward origin and by the stable or uniform temperatures commonly found along a Santa Ana boundary. Santa Ana wind events also tend to quickly manifest, so a case involving them was found with a rapid increase in intensity on the time scale of six to eight hours. This window may allow the traditional output of the HDW to indicate a rise in risk. However, the more refined temporal output from the HRRR model could be used to indicate more precisely the increased risk.

The data for this case were then analyzed using the method from Srock et al. (2018), then modified to run using HRRR data as inputs; the output files were saved as network common (.nc) files. A control run utilizing the original HDW code and a CFsV2 dataset was made to provide a baseline to determine any improvements or decline in the performance of the HRRR model outputs.

By the nature of the HRRR model, hourly outputs for the HDW index can be produced, which delivers six times the temporal resolution over the original HDW index. This is critical as a forecasting tool, because more lead time or advanced warning can lead to a more successful protection of human life, structures and other resources, including the firefighting equipment itself.

For this study, the CFsV2 model was run at its native output resolution of 0.5 x 0.5 degrees. The HRRR data was run in its native spatial resolution of 3 x 3 km. Both models were run over the same domain to maintain a continuity in comparison of the results. Both models use a similar structure for the vertical resolution, with each model taking between 20 and 25 vertical levels. Therefore, the method for evaluating the conditions within the lowest few levels of the model was the same for both the HRRR and CFsV2 outputs, so no special considerations needed to be made in the z-axis.

There is a strong diurnal cycle that is present in the maximum values for the HDW index. This follows the fact that in most locations at most times of the year, the temperature falls during the nighttime and rises during the daytime due to solar heating. This variation has a large impact on the vpd. Also, due to the reduction in differential heading, the winds tend to calm during the night. With the HDW defined as it is, these factors create the strong diurnal cycle that is observed and explain why Srock et. al (2018) did not analyze the HDW for the 0000 UTC output.

Results and Analysis

A comparison of the images produced by the CFsV2 and HRRR datasets yields several interesting results. Upon initial observation, the first and most noticeable feature is in the

texture of the outputs between the climate reforecast model and the high-resolution mesoscale model. The climate model has much blockier and general output values. This is to be expected as focusing on such a small area is not what the CFsV2 model outputs were designed to capture on neither the spatial scale of the large wildfire or the 3 days being sampled and is easily seen in Figure 16. This is the spatial area and times for which HRRR models are built and is easily seen in Figure 17; textures in the outputs that are beginning to capture the terrain effects of the coastal mountain ranges that even on the 3 km grid are still on the sub-grid scale.

Throughout the analyses, both models have the highest values consistently to the south and east of the historical event. In Figure 16, the peak values of the HDW Index are indeed to the southwest of the peak burn area. This is consistent with the damage seen in Figure 1. The fire originated 5 days earlier to the southwest of the point designated in Figures 16 and 17. This makes the HDW Index analysis more credible as the area indicated as having a high HDW Index value was either burning or had already burned. Another factor that contributes to the spatially skewed values is that the conditions throughout all of southwestern California were hot and dry and therefore susceptible to wildfire; this area just happened to receive the spark in the form of a transmission line failure and was one of a complex of several wildfires burning in the region at this time.

Another feature that was consistent between the two models was that the HRRR output had much higher values for the HDW Index on nearly every image. This is also likely an artifact of the scales of the data being used coupled with the model's individual capabilities. It is important to note the significance of these differences. On the large scale the CFsV2

Following a conversation with the HDW's lead author, artificially low values found near the coasts have been reported by users. This information is also consistent with the findings of this study. This artificially low value is of greater impact in the CFsV2 outputs, given the much larger spacing between grid squares, and is thought to be related to the land/ocean interface of a shared grid square in the model outputs. This artifact is also present in the HRRR outputs of the HDW Index, but the effect is lessened due to the much smaller 3 km grid spacing. For the CFsV2 HDW output, the lower values are likely driven by the model grid sharing a land-ocean interface, so temperature and humidity values averaged over the grid will be modified from the purely overland cells.

While the times associated with sunrise and sunset are not entirely critical from a maximum of the HDW index standpoint, the HDW Index values are early in the day, between the 6-hourly output window using the CFsV2 window can assist a wildfire manager in making some key decisions with regard to manpower and equipment placement earlier in the day. This is an advantage provided by the HRRR dataset that is not present when using the CFsV2 data.

The maximum values found by the HRRR HDW Index outputs for this time have a value between 350-400 and are already exceeding the Climate Forecast System Reanalysis (CFSR) Climatological values from McDonald et. al (2018) 95th percentile value of the HDW Index. This highlights an exceptional risk, verified by the wildfire having already burned approximately 159,000 acres. Using the CFsV2 data, the values are much lower, falling around the 75th percentile, indicating an enhanced wildfire risk, but not nearly as severe as was both observed and indicated in the HRRR HDW Index output.

Use of the HRRR model data may also help in preventing disasters such as the Yarnell Hill fire of 2013. The HRRR model is a convection-allowing model and may have indicated the convective outflow boundary identified by the Serious Accident Investigation Report (2013) that was the cause of and rapid intensification and spread that doomed the Hotshot crew. This feature is another improvement over the original CFSv2 data which does not allow convection.

Moving to the 1200 UTC analysis of the HDW Index for December 9th, the decrease in values of the HDW Index overall should be noted. This is the early morning on the west coast and is a good representation of the minimum value for the day. From the previous image, the values over the city of Los Angeles have decreased. The HRRR output follows a generally similar pattern, with the higher terrain of the coastal range outlined with higher values. Additionally, the area directly to the east of the location noted on Figure 19 shows higher values, greater than 150. This is at or above the 50th percentile per the HDW climatology completed by McDonald et. al (2018) for this area. The local METAR for the nearest airport, Oxnard, CA (Found in Appendix IA) was not indicating any of the traditional threats such as wind, with the 1200 UTC observation were still only six knots. The winds would accelerate rapidly in the following few hours, first meeting the criteria proposed by Small (1995) at the 1700 UTC observation, with a station pressure difference of 0.34 inches of mercury or 11.51 hPa. This marks the beginning of the SAW conditions that would last for approximately the next 30 hours which is in general agreement with findings from Raphael (2003), which noted that SAW events were on average 1.5 days in duration.

The timing of the SAW event beginning around midday is another ingredient for the large values of the HDW Index. The first signs of this are found on the 1800 UTC CFsV2 and HRRR outputs (Figures 20 and 21, respectively), with the highest values recorded to this period in the study. Within Figure 21, the maximum values clearly represent the area that had burned on December 5th, the first day of the wildfire event. This figure also clearly shows the area that did not burn (seen in Figure 1) as having an HDW Index value that is lower than 50, which represents almost no risk of wildfire spread whatsoever. At this time, the area on a line to the northeast of the point depicted as the burn area of December 10th is showing an increased value for the HDW Index, with values between 200-300. This is an increase from 18 hours earlier in which the values

ranged from 50-150 and should be interpreted as a strong signal of increased wildfire spread risk to this area.

For the 0000 UTC CFsV2 and HRRR outputs (Figures 22 and 23 respectively) on the 10th. The CFsV2 analysis is showing no signals of any kind, which is odd given the strong winds observed at this time. This is likely another artifact of the climatological dataset with coarser spatial resolution. The wind likely was much lower along with lower air temperatures over the open ocean creating an artificially low value for the area over land. This contrasts with the HRRR output which indicates high values in the areas that have already burned. This is in agreement at this time with the CFsV2 output for a low fire spread risk and the values matching the CFsV2 output with HDW Index values primarily in the 50-100 range.

At 1200 UTC for both the CFsV2 and HRRR output (Figures 24 and 25 respectively), HDW Index values are increasing. However, the location of the increase for the CFsV2 output is to the northeast, likely representing the enhanced winds and increased temperature in the mountain ranges. The HRRR output's signal is much stronger and widespread, with values increasing around the area depicted as the center of the burn area. These values have increased from 50-100 to over 200.

Most exciting of the results for this study come from the 1800 UTC outputs. The strongest signal from the CFsV2 analysis (Figure 26) shows a broad corner with values between 50 and 100. Further to the northeast, the values increase to a maximum of 100-150. This is agreed with and enhanced by the values from the HRRR output (Figure 27). The maximum values approach 500. There is a widespread area of high values, both in the formerly burned area and in the area of the designation with values greater than 350 but less than 400. This image also very clearly denotes the area of Lake Casitas and the area to the north-northeast which was spared from burning as having HDW Index values below 50.

As was noted in the meteorological analysis, the 0000 UTC outputs from the HDW Index still have some elevated values. This is the first time the CFsV2 image has a good grasp of the precise location of the wildfire threat. The CFsV2 analysis (Figure 28) has an area centered around the mark denoting the area burned on December 10th. These values are greater than the background values with readings of 50-100. Finally, the HRRR analysis (Figure 29) is still showing enhanced values greater than they had been, however as noted in the meteorological analysis, the conditions for wildfire spread were just beginning to weaken at this time and the values are still heightened in the proper areas, are reduced from their maximum values six hours earlier.

Conclusion

The results show that utilization of the HRRR model does improve the usability and accuracy of the HDW Index when analyzing a historic wildfire event. The HRRR is a modern and a currently used model, and there are many sources available to wildfire managers to receive this information very shortly after its production. This contrasts with the CFsV2 data, as that dataset is a forecast reanalysis, requiring the forecast period in question to have already passed. Additionally, the reforecast data also takes time to be processed, further lagging the availability to the user. Utilization of the HDW with HRRR model output data will allow a fire manager some means of "getting ahead" of an event in progress. Future possible research includes analyzing a more complex case. This could include a case involving a mid-latitude cyclone where both a moisture and wind gradient are present, like a plains fire in the central United States, and applying the model to a higher spatial resolution. This would be possible with HRRR model data since resolutions of 0.25 x 0.25 degrees may start to provide threat information for individual canyons and other high hazard and threat areas. This would be a method of measuring the local effects of terrain and other effects found at lower scales. Further shortening the time steps could be another study, to try to find if there is a significant benefit to half-hourly outputs as opposed to the hourly that is available in this study. This would not be difficult to accomplish given the HRRR model is capable of running to half-hourly time steps. Two separate comparisons could then be made and an ideal solution for temporal and spatial resolutions could be found.

To further make the HDW Index an operational product, a hazard warning level would be generated based on pairing the HDW Climatology work done by McDonald et. al (2018) with the HRRR output. Currently, the HDW Index product in use by the 25 OWS has warning flags issued based only on brief observation of low, medium, high, and extreme values.

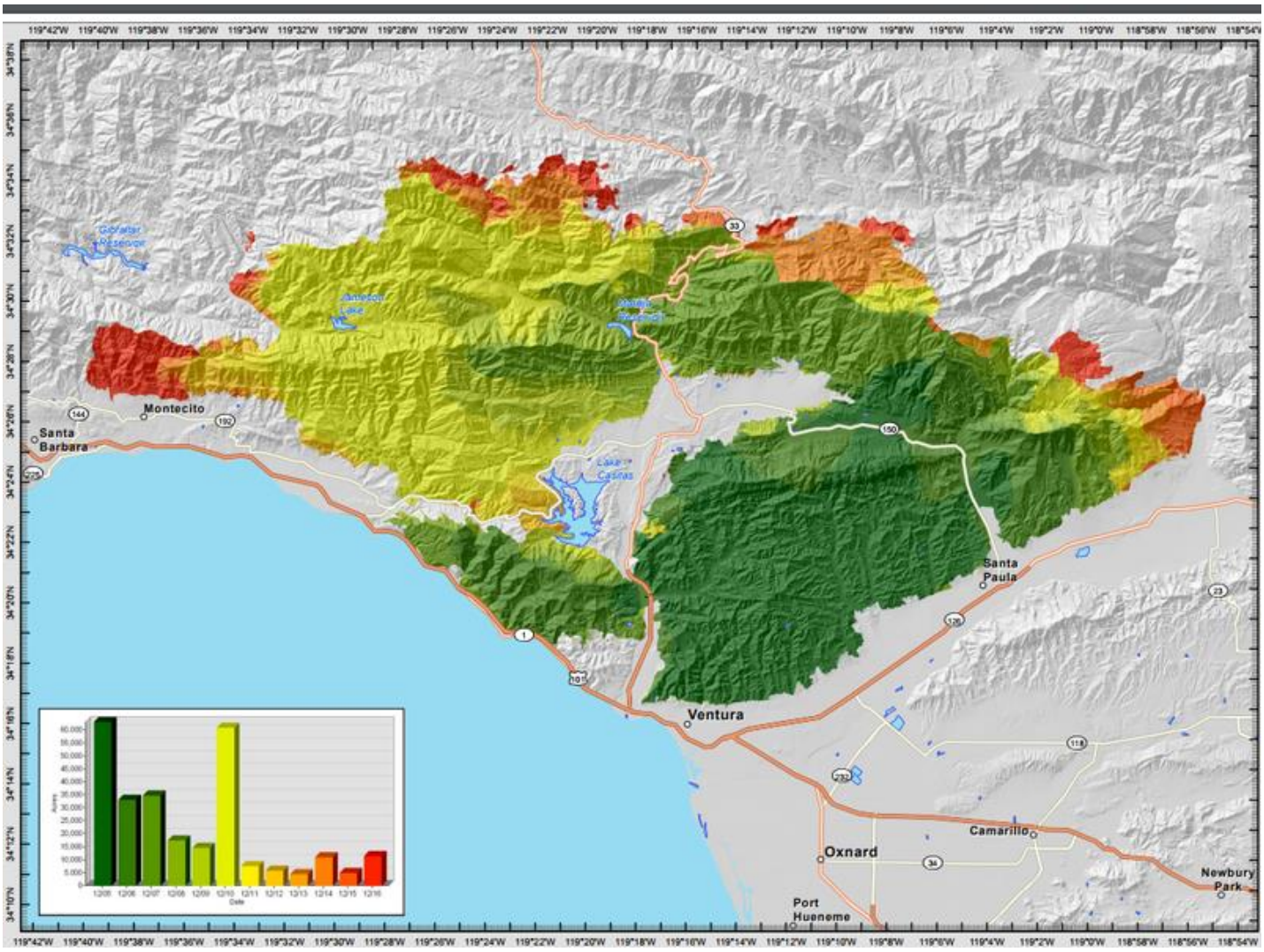

Figure 1. Image depicting the burn area of the Thomas fire of December 2017. Note the large burned area increase over the previous and subsequent day, colored yellow, representing December 10th.

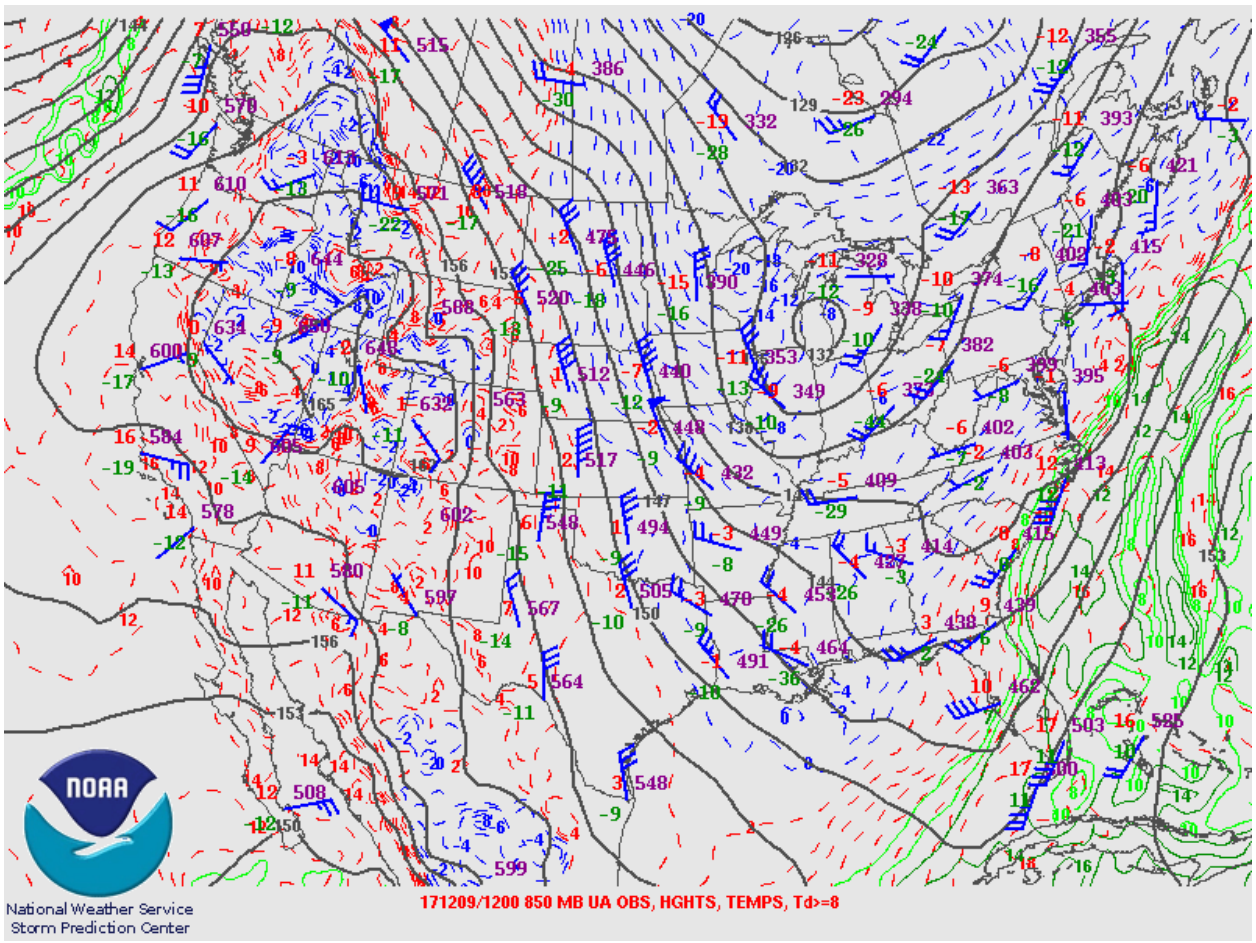

Figure 2: 850 hPa analysis for 1200 UTC December 9th, 2017. Note the cyclonic rotation immediately offshore in the Los Angeles, CA area. Image courtesy of NOAA Storm Prediction Center (SPC) archive.

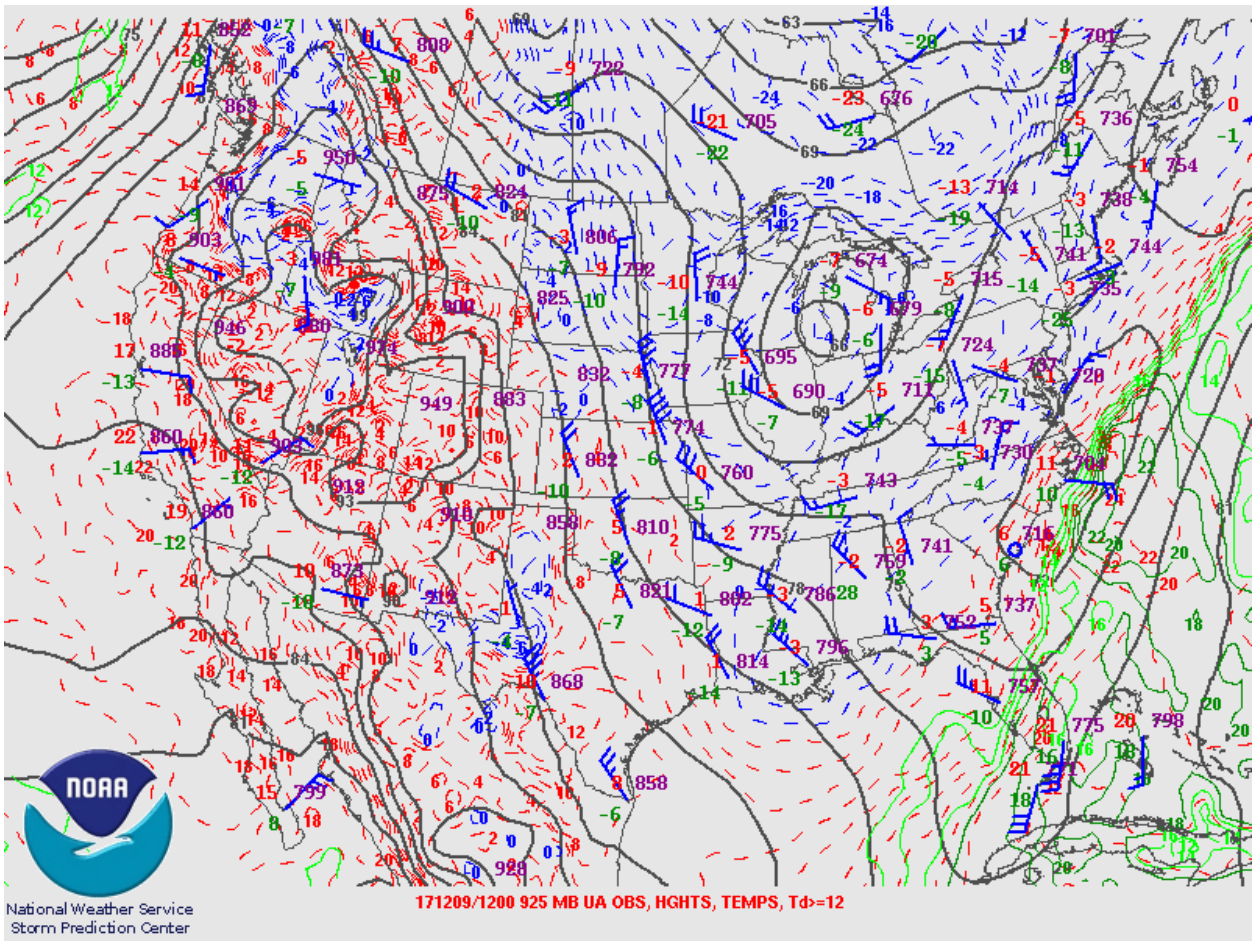

Figure 3: 925 hPa analysis for 1200 UTC December 9th, 2017. Note the stronger temperature and pressure gradient parallel to the Sierra-Nevada mountains. Note that due to the elevation of the Sierra-Nevada range, the 925 hPa level may be at or below ground level in some areas on this map. Image courtesy of NOAA SPC archive.

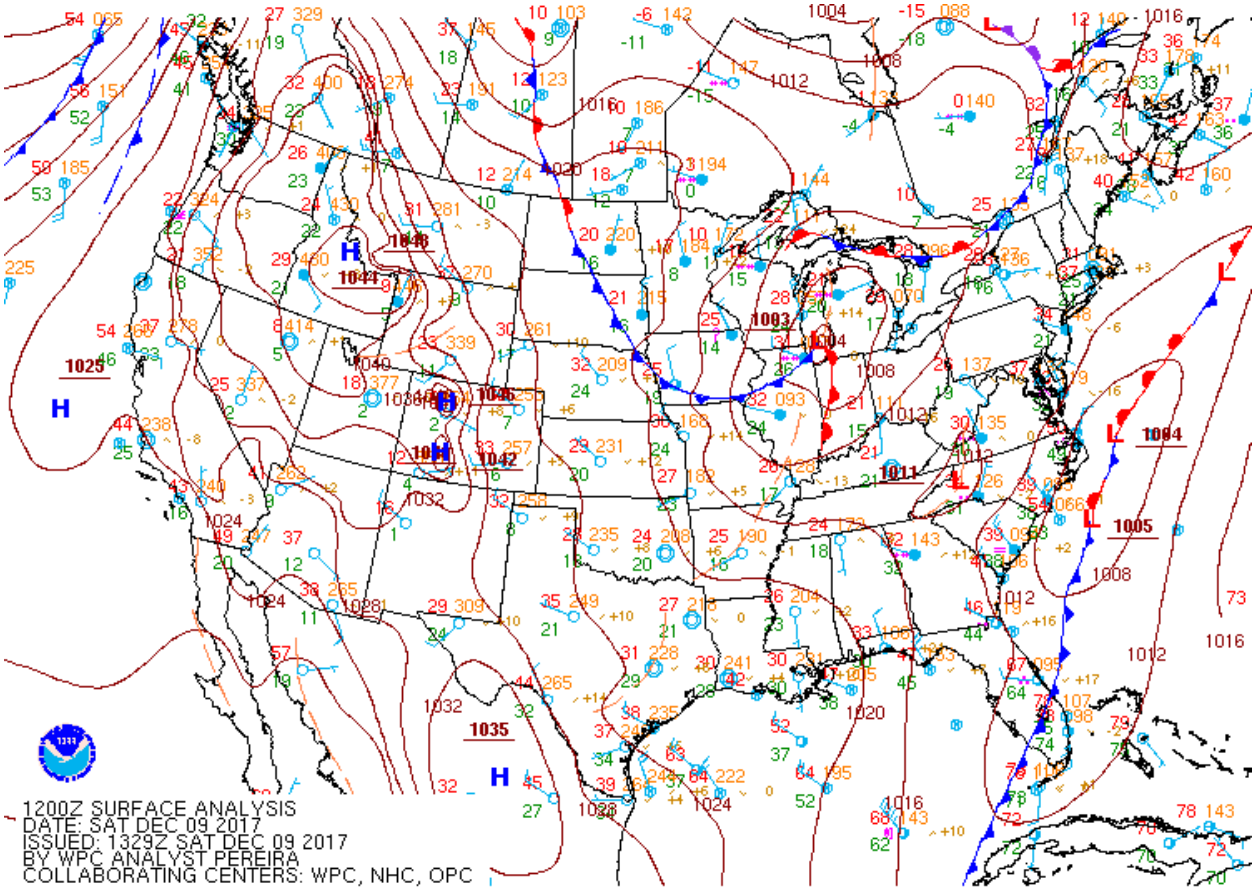

Figure 4: Surface analysis for 1200 UTC December 9th, 2017. Note the highly localized pressure gradient just northeast of the Los Angeles area. Image courtesy of NOAA Weather Prediction Center (WPC) archive.

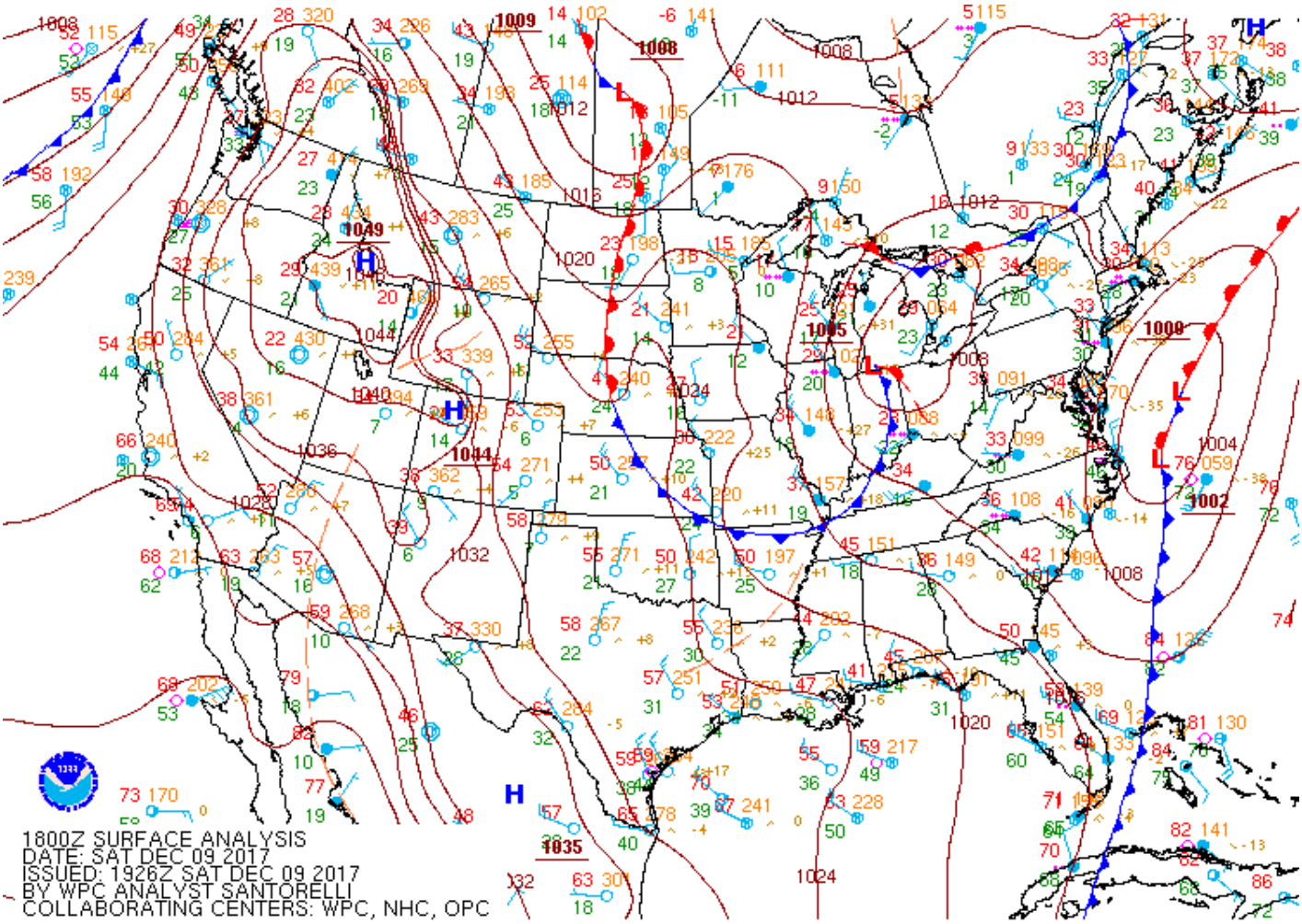

Figure 5: Surface analysis for 1800 UTC December 9th, 2017. Note the broad area of strong high pressure in the Great Basin region. It is also noteworthy to see the 27°F temperature difference between Tonopah, NV and Los Angeles, CA. Image courtesy of NOAA Weather Prediction Center (WPC) archive.

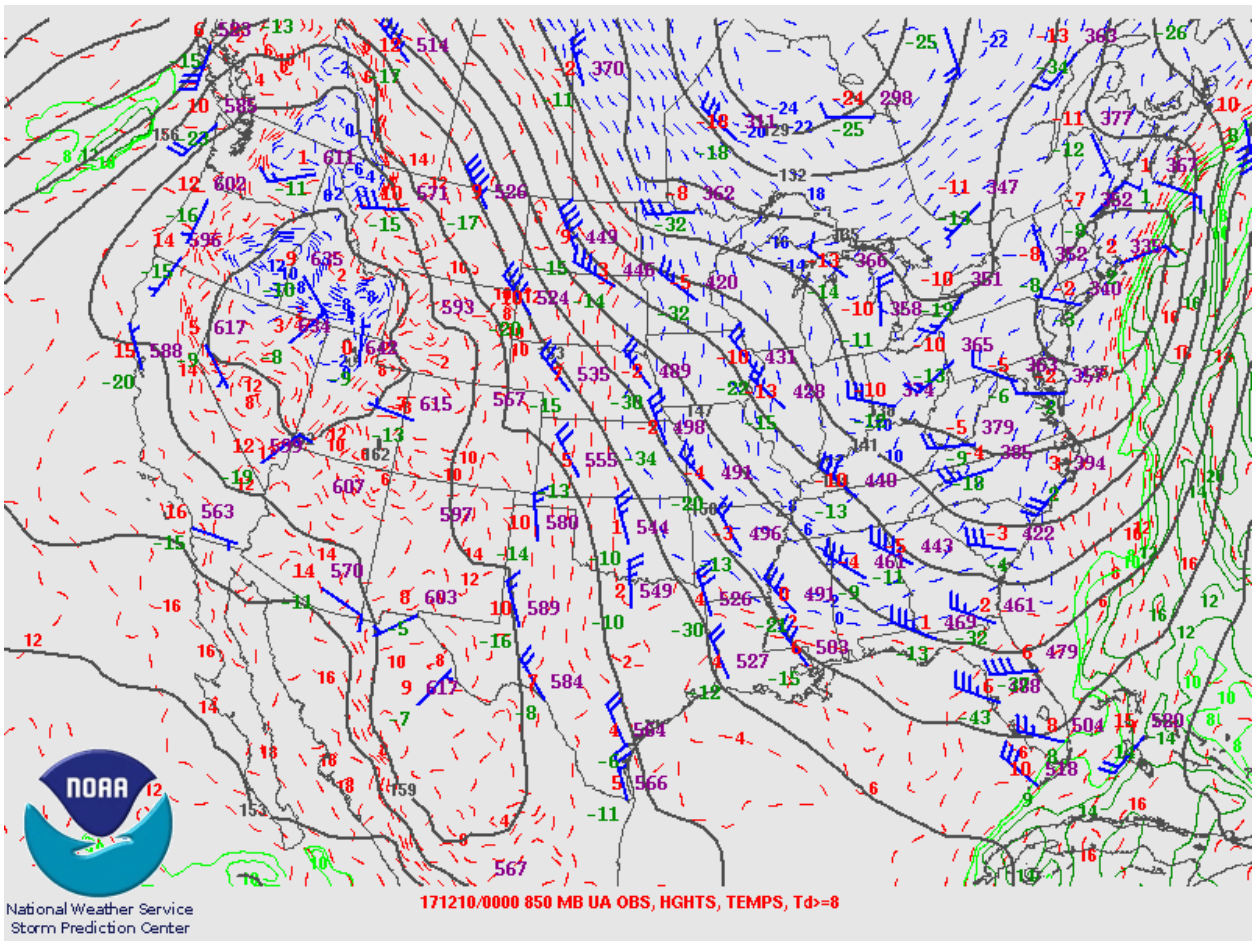

Figure 6: 850 hPa analysis for 0000 UTC December 10th, 2017. Note the broadening of the high pressure in the great basin region while maintaining a ridge into British Columbia, Canada. Image courtesy of NOAA SPC archive.

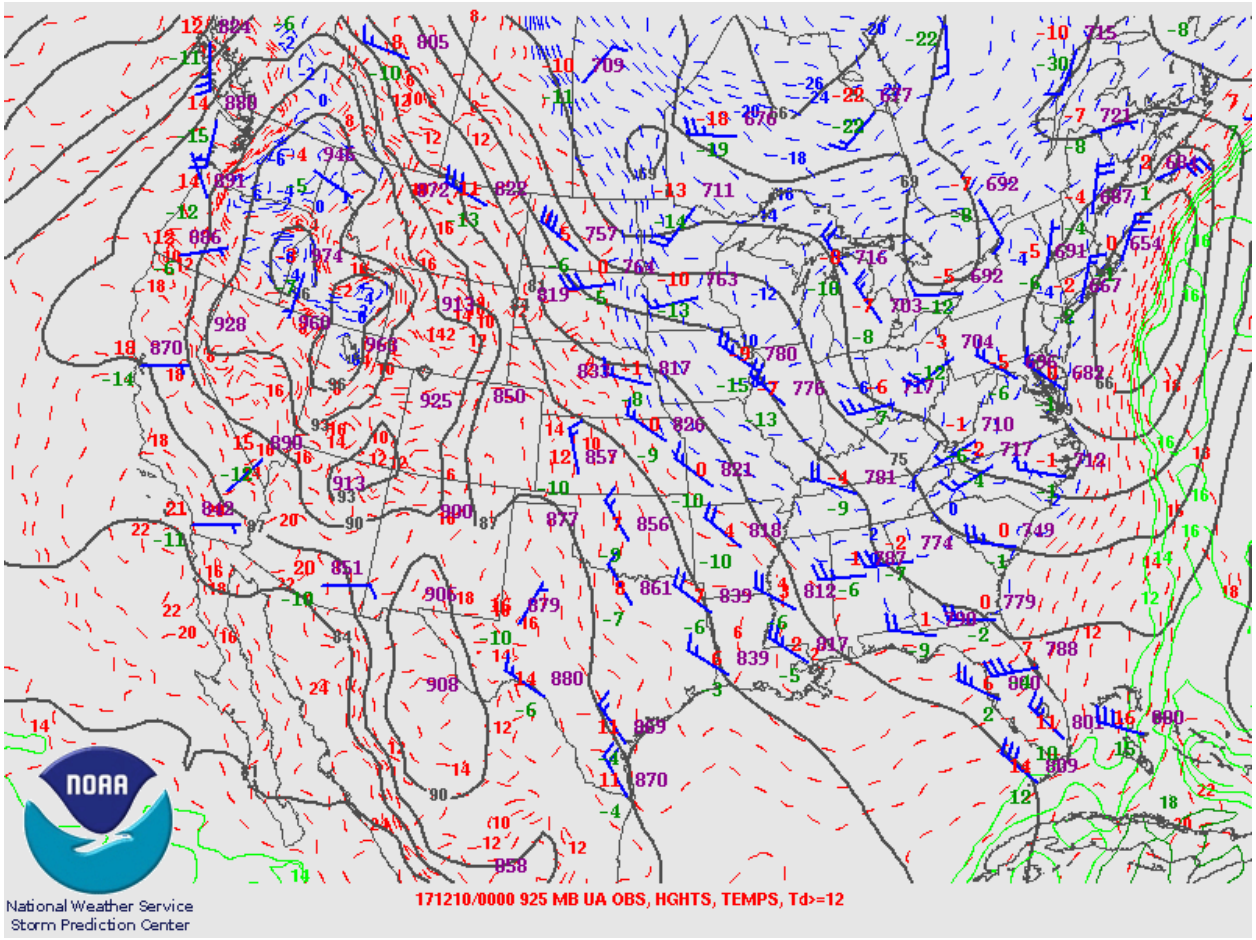

Figure 7: 925 hPa analysis for 0000 UTC December 10th, 2017. Image courtesy of NOAA SPC archive.

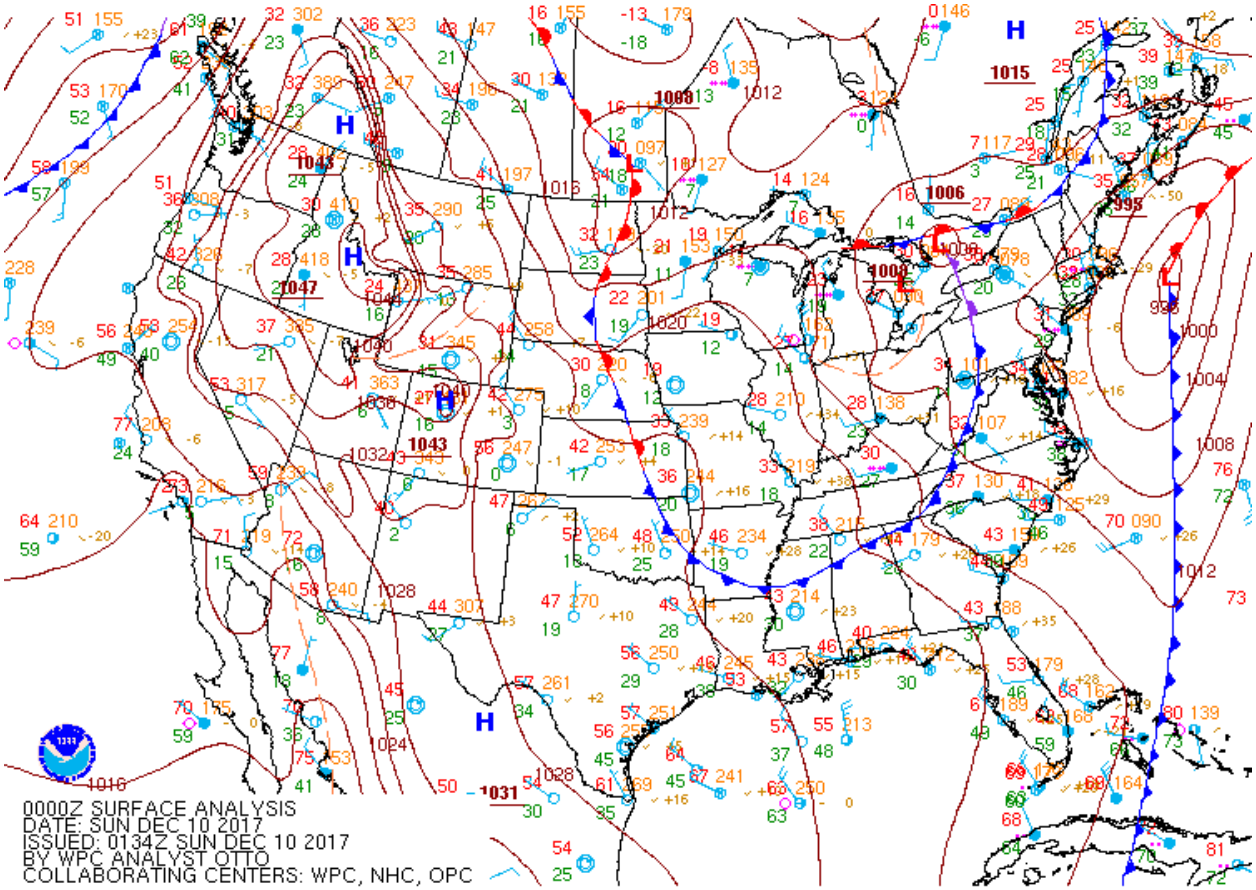

Figure 8: Surface analysis for 0000 UTC December 10th, 2017. Image courtesy of NOAA WPC archive.

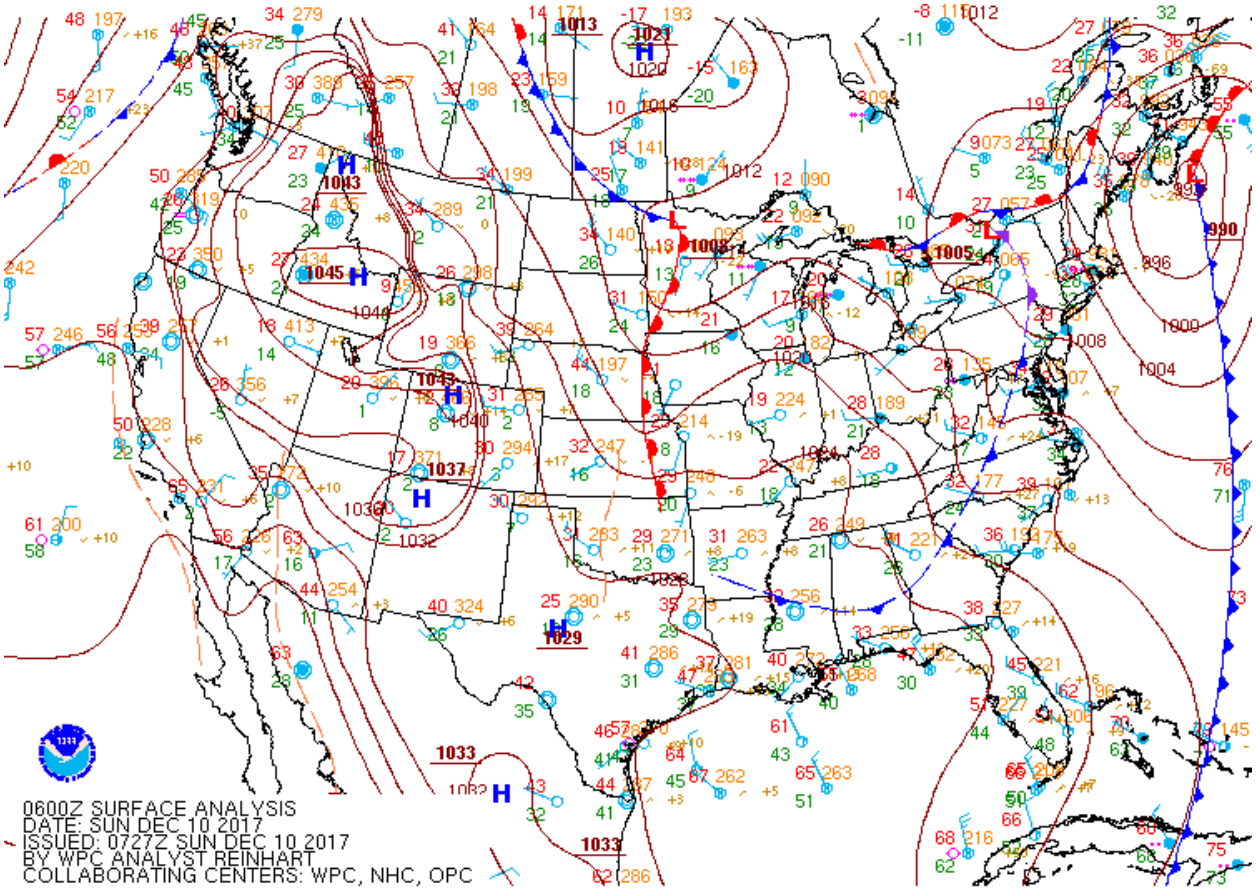

Figure 9: Surface analysis for 0600 UTC December 10th, 2017. Note the addition of the trough notation by the analyst for the first time at this time. Also note the pinching of the pressure gradient directly northeast of the area of the wildfire in California. Image courtesy of NOAA WPC archive.

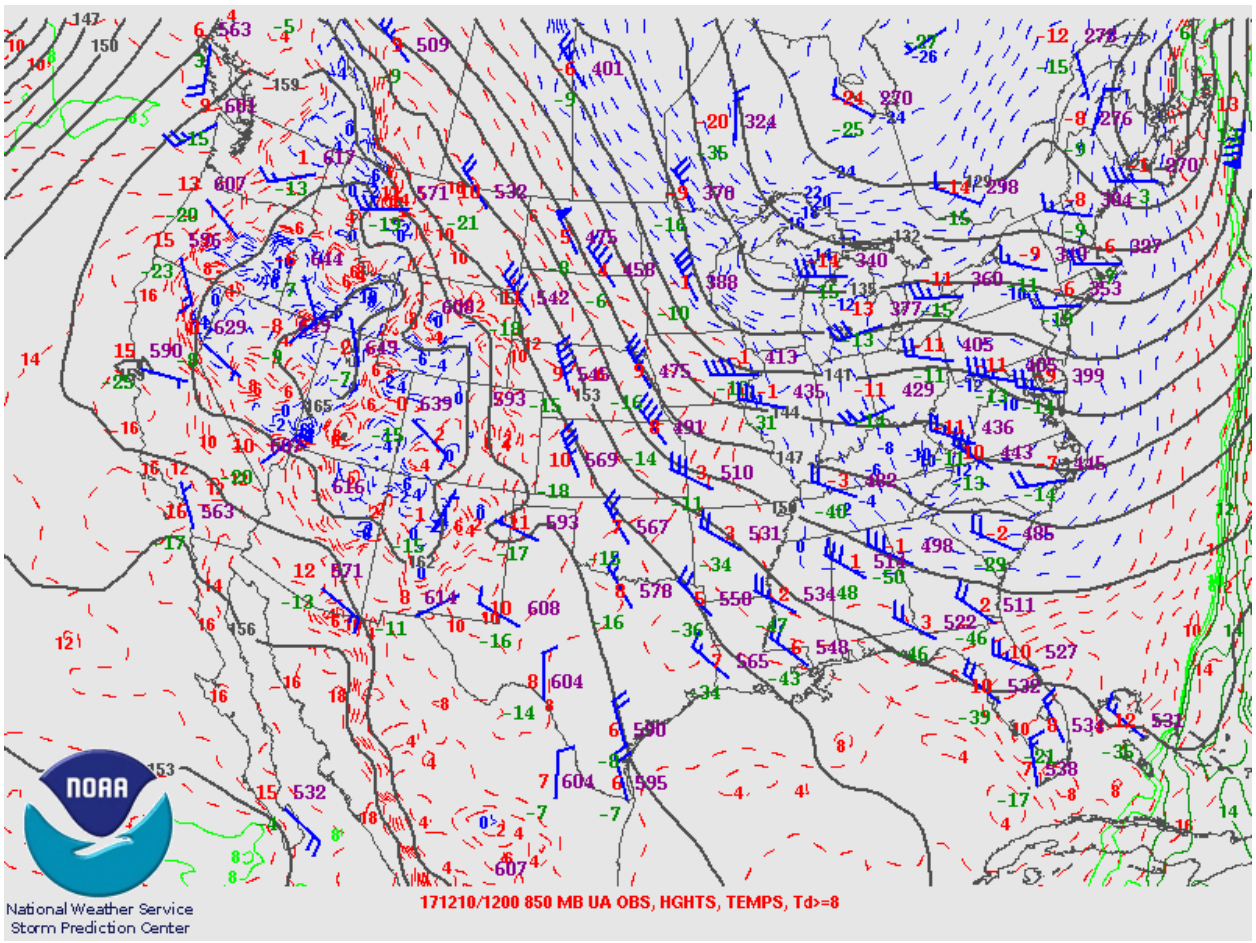

Figure 10: 850 hPa analysis for 1200 UTC December 10th, 2017. Note the southerly shift of the high pressure from southern Idaho to the eastern border of Utah with Nevada. Image courtesy of NOAA SPC archive.

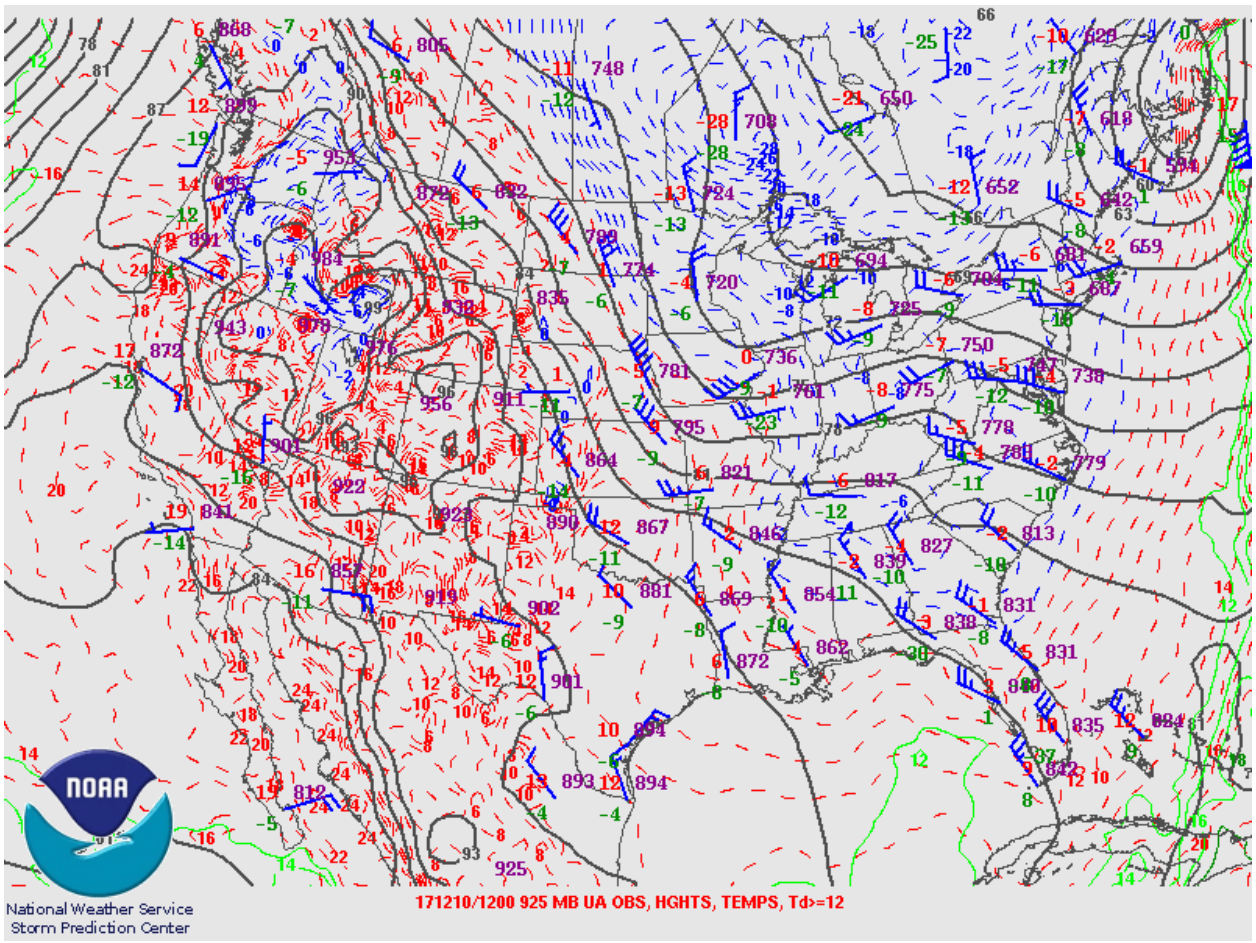

Figure 11: 925 hPa analysis for 1200 UTC December 10th, 2017. Note the tightening of the pressure gradient between Los Angeles, CA and Tonopah, NV, particularly along the Nevada-California border at this time. Image courtesy of NOAA SPC archive.

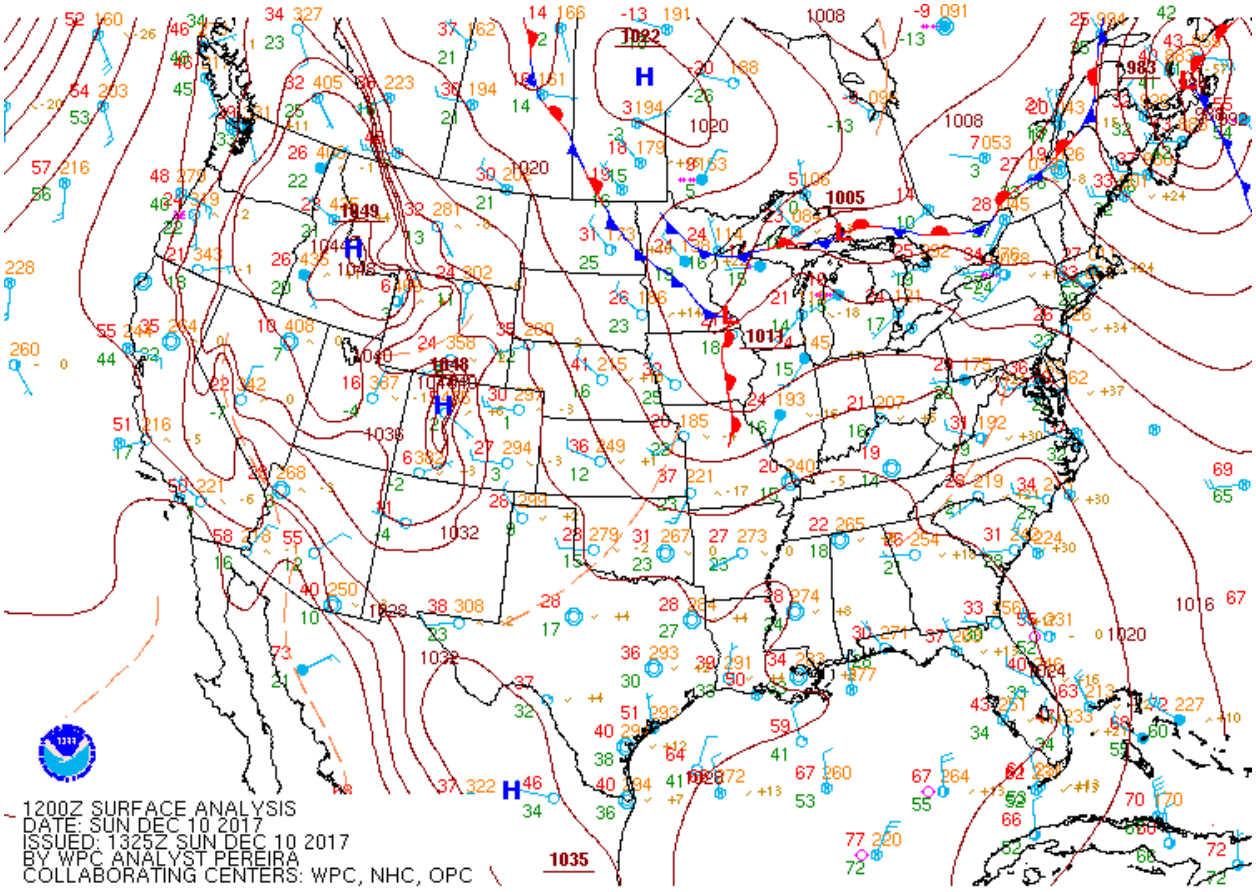

Figure 12: Surface analysis for 1200 UTC December 10th, 2017. Image courtesy of NOAA WPC archive. Note the southerly shift of the high pressure from southern Idaho to the eastern border of Utah with Nevada.

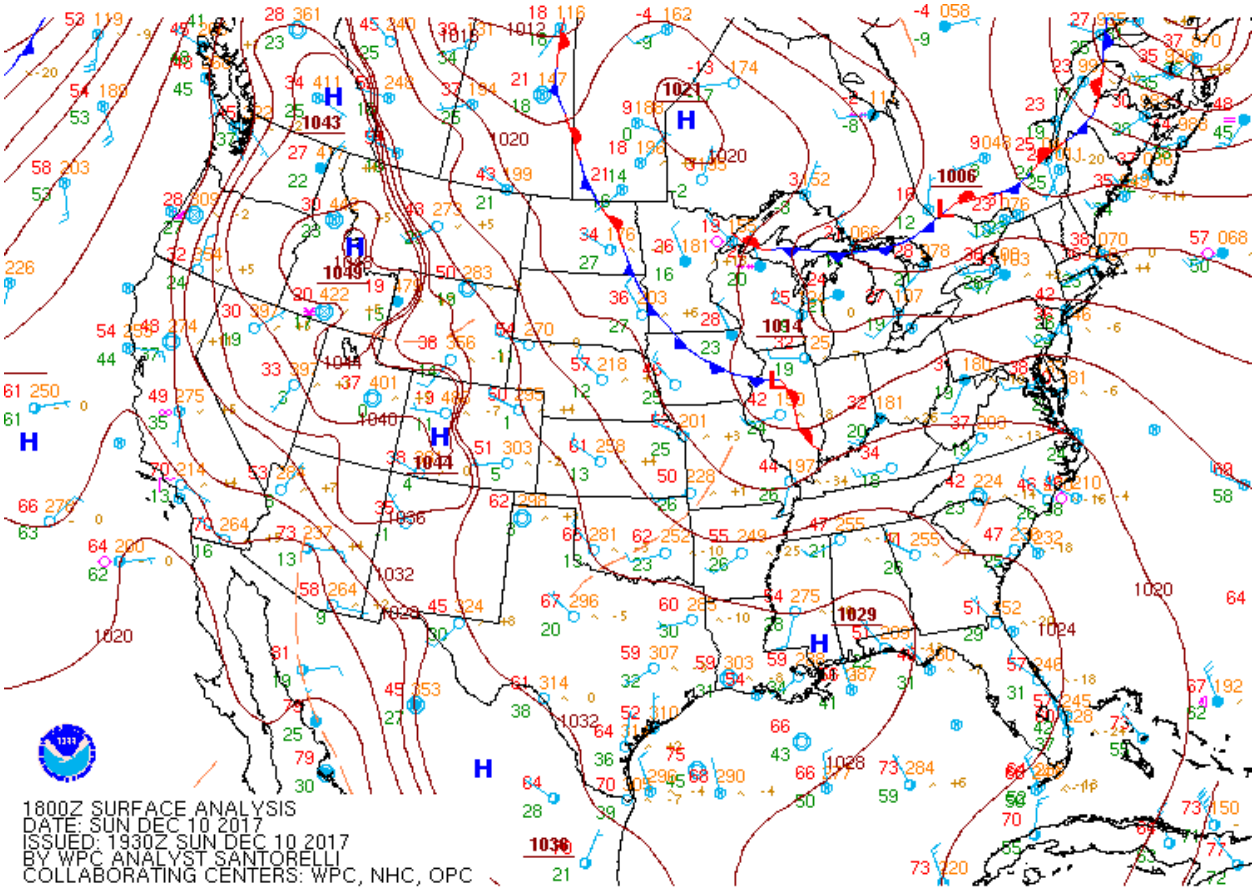

Figure 13: Surface analysis for 1800 UTC December 10th, 2017. Image courtesy of NOAA SPC archive. Note the southerly shift of the high pressure from southern Idaho to the eastern border of Utah with Nevada.

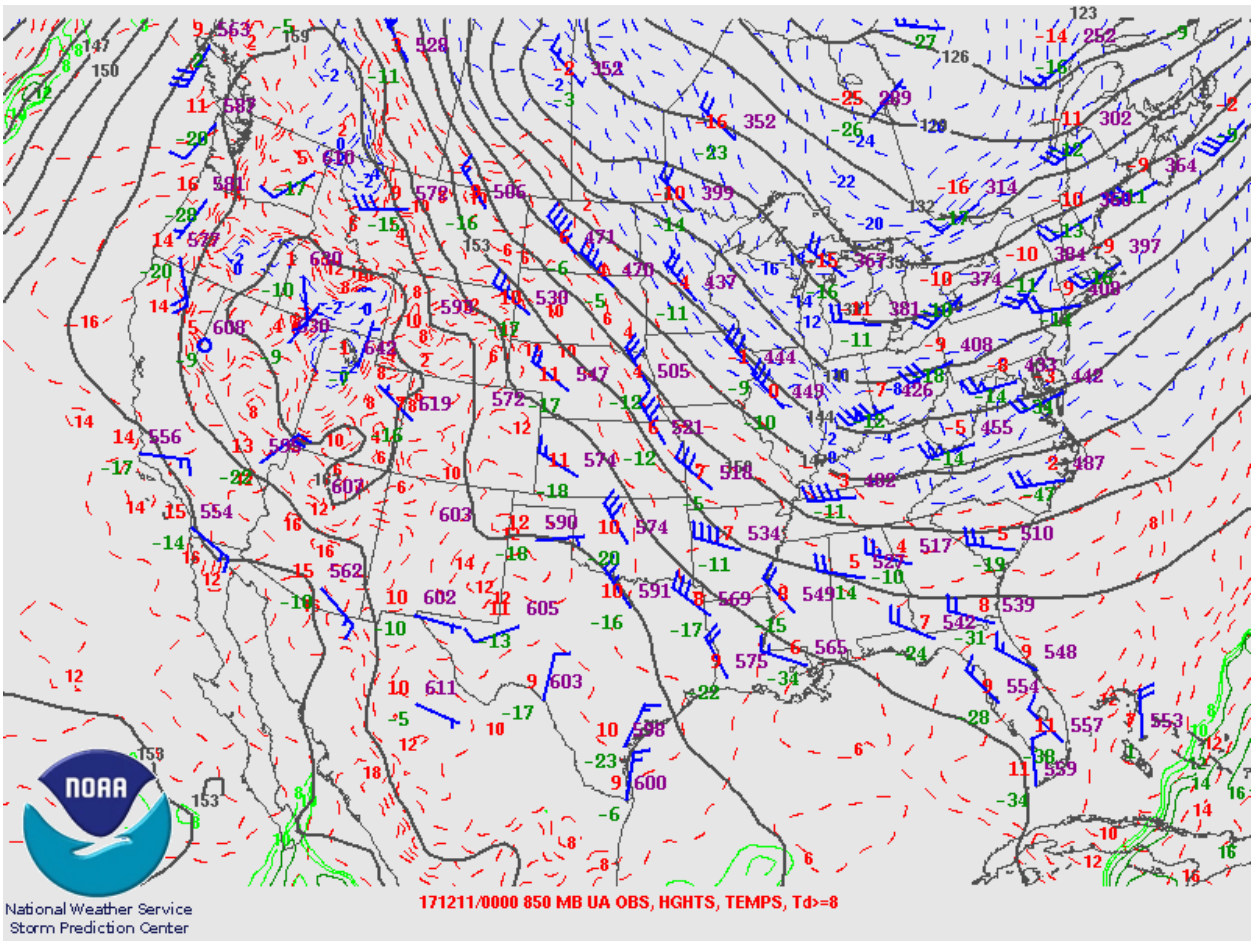

Figure 14: 850hPa analysis for 0000 UTC December 11th, 2017. Image courtesy of NOAA SPC archive. Note the southerly shift of the high pressure from southern Idaho to the eastern border of Utah with Nevada.

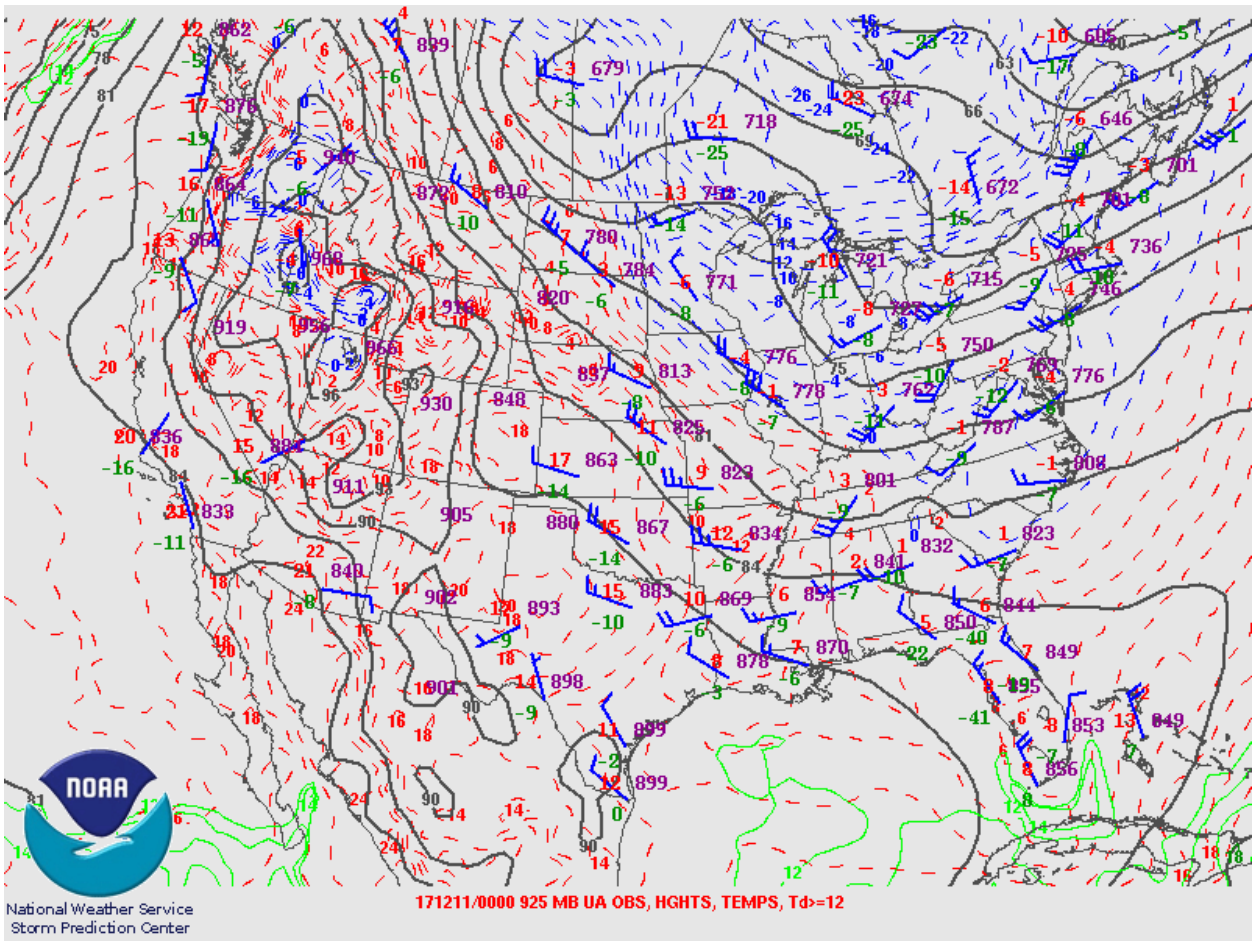

Figure 15: 925hPa analysis for 0000 UTC December 11th, 2017. Image courtesy of NOAA SPC archive. Note the southerly shift of the high pressure from southern Idaho to the eastern border of Utah with Nevada.

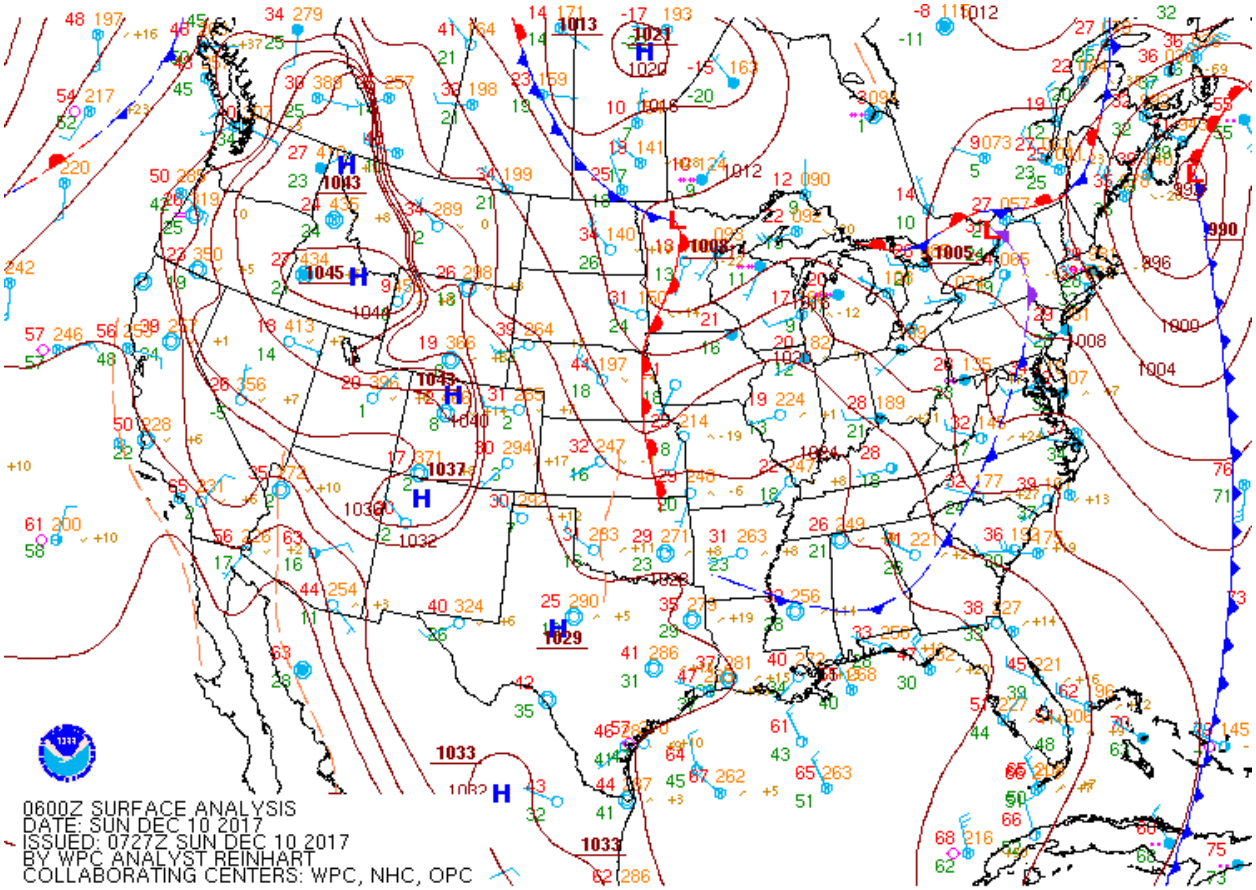

Figure 16: Surface analysis for 0600 UTC December 11th, 2017. Image courtesy of NOAA WPC archive. Note the southerly shift of the high pressure from southern Idaho to the eastern border of Utah with Nevada.

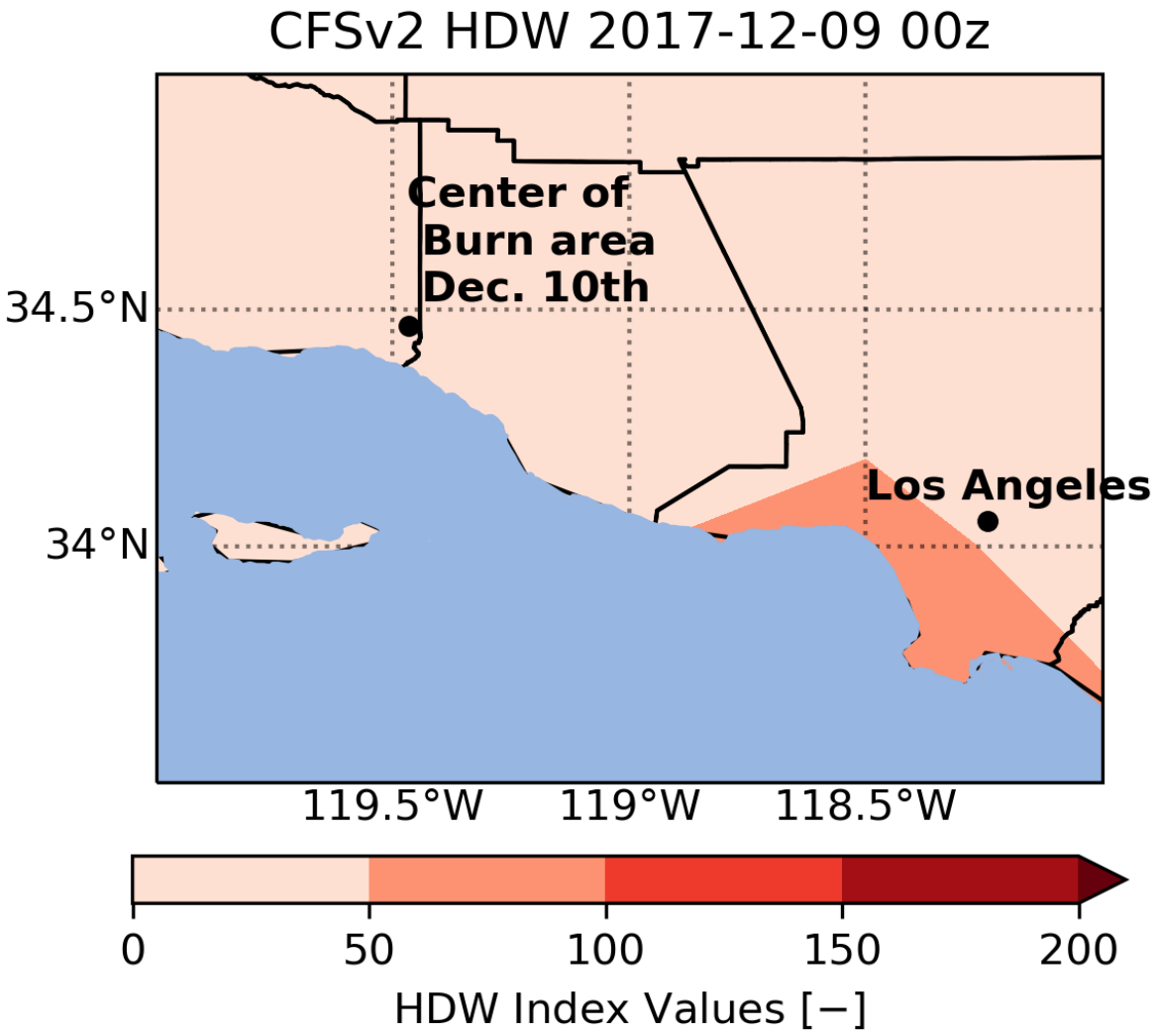

Figure 17: CFSv2 HDW map of the area burned for December 9th, 2017 at 0000 UTC. A position marker for the center of Los Angeles, CA is added for reference.

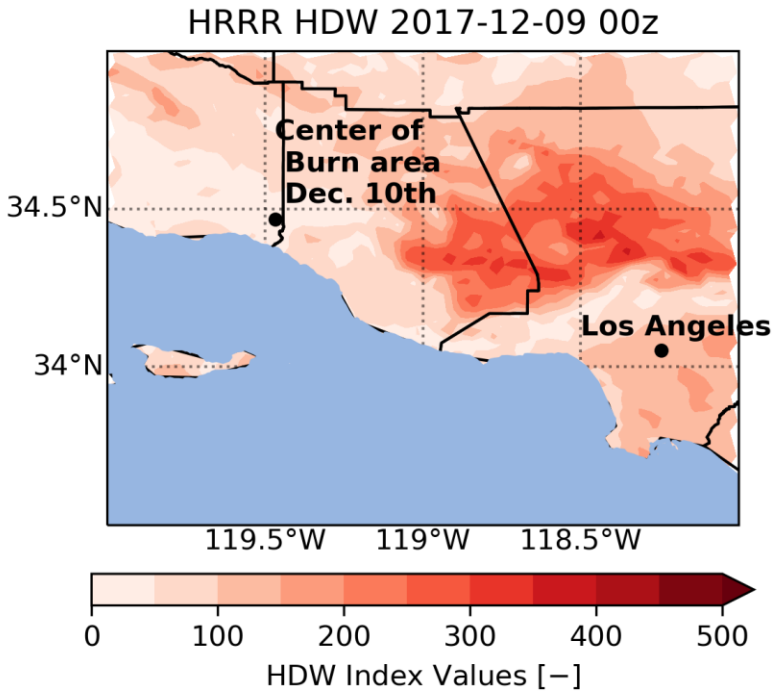

Figure 17: HRRR HDW map of the area burned and Los Angeles area for December 9th, 2017 at 0000 UTC.

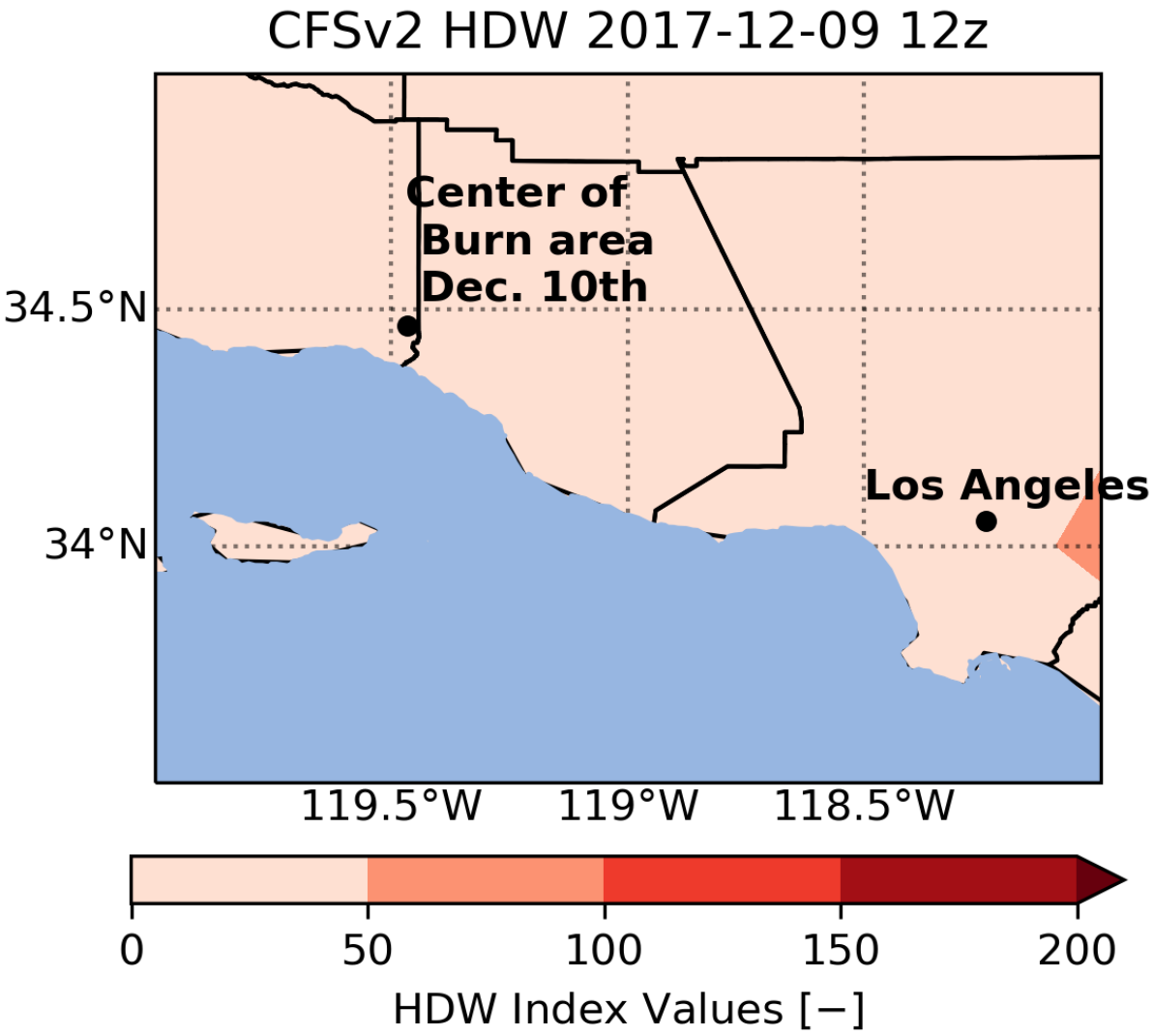

Figure 18: CFSv2 HDW map of the area burned and Los Angeles area for December 9th, 2017 at 1200 UTC.

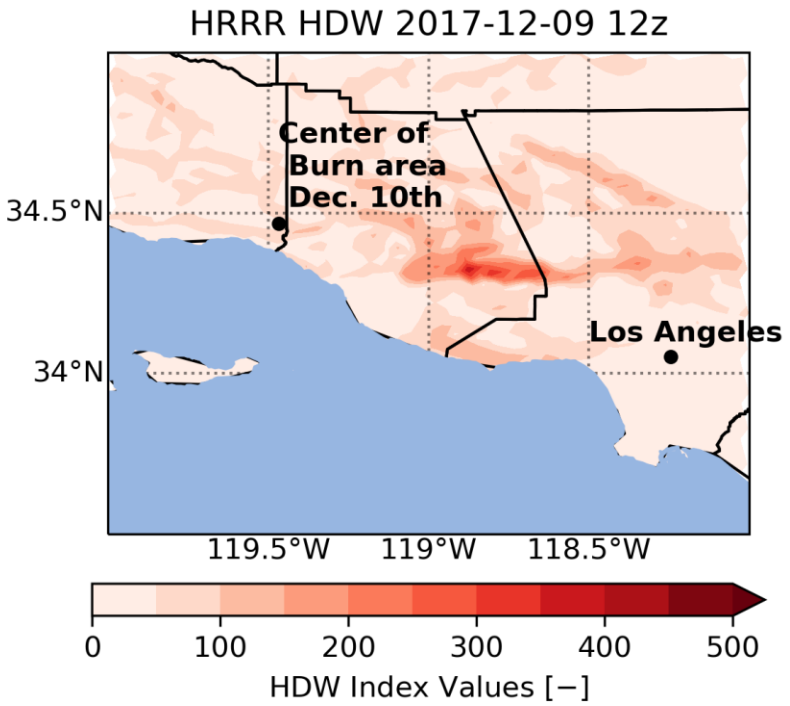

Figure 19: HRRR HDW map of the area burned and Los Angeles area for December 9th, 2017 at 1200 UTC. This is near daybreak for this location. Note the increased activity to the east-southeast of the area that had yet to burn.

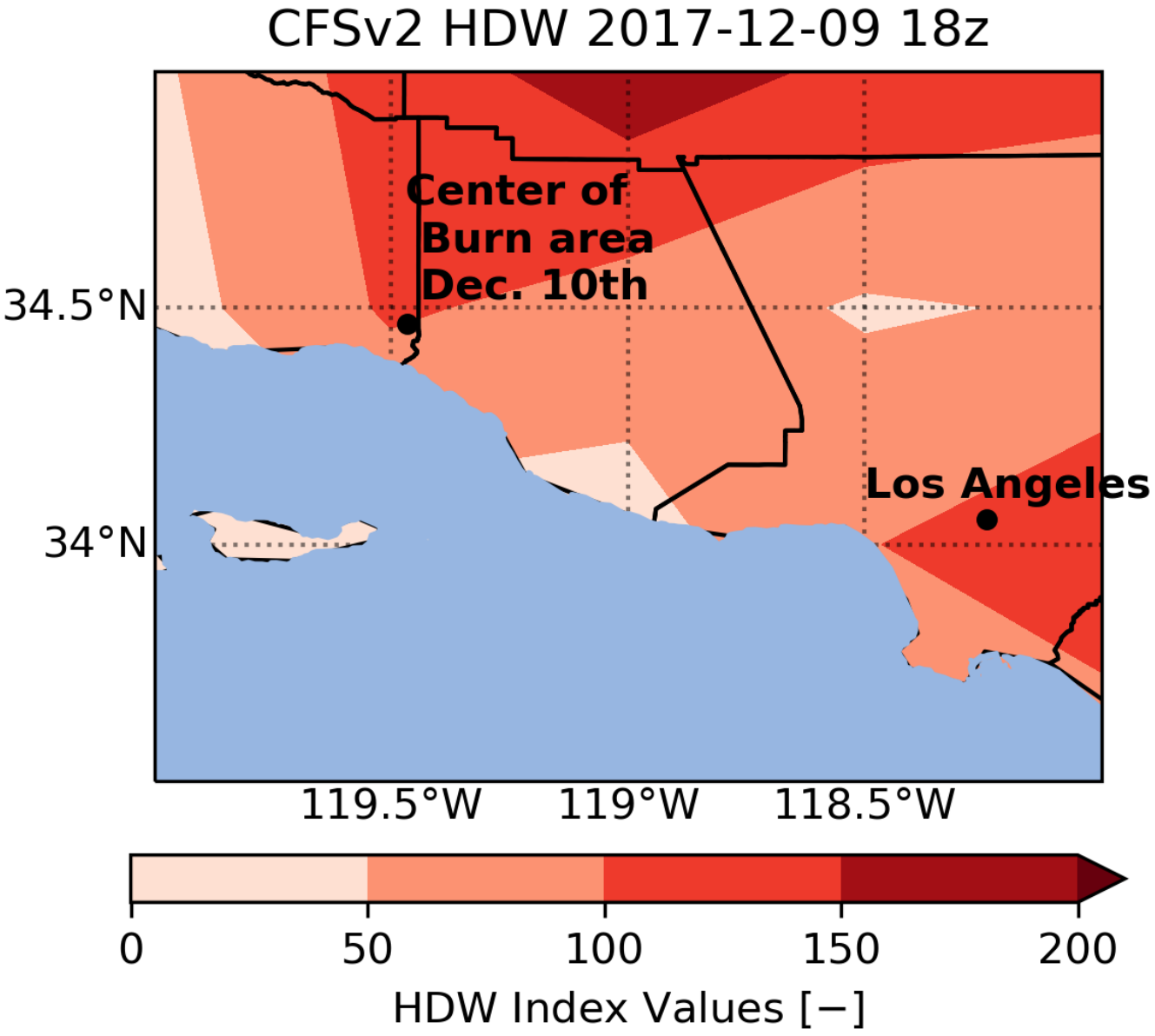

Figure 20: CFSv2 HDW map of the area burned and Los Angeles area for December 9th, 2017 at 1800 UTC.

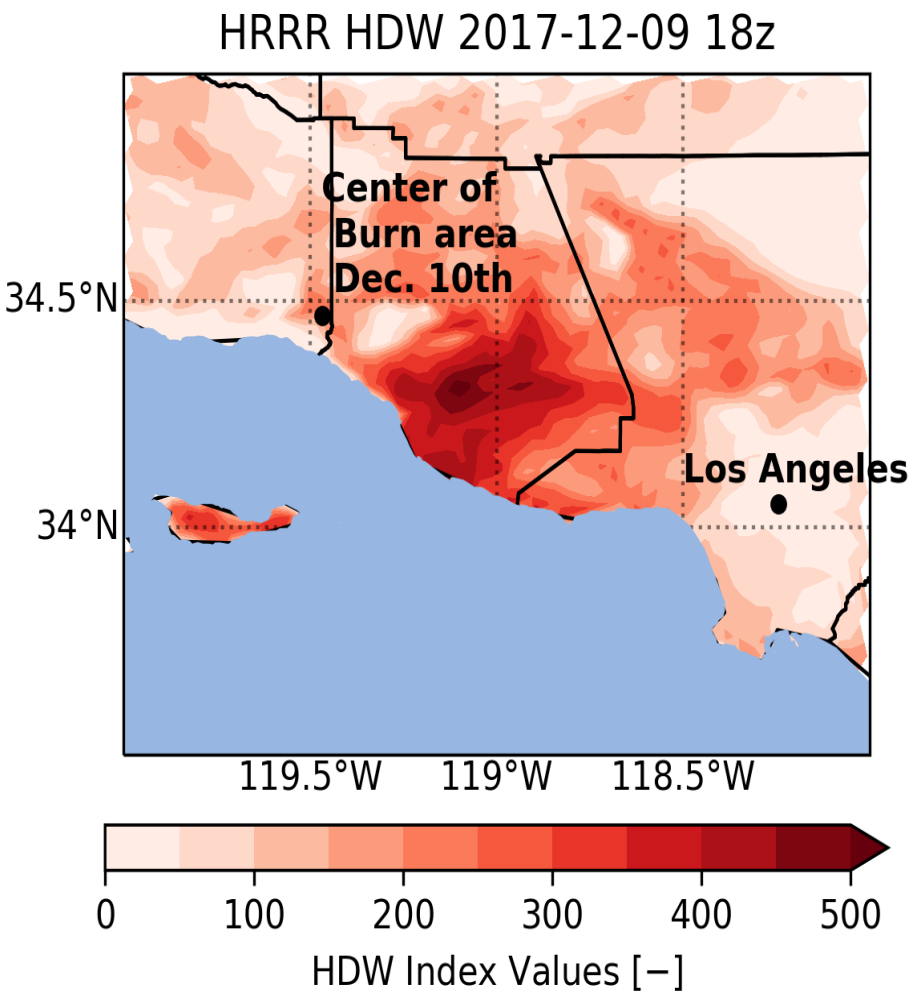

Figure 21: HRRR HDW map of the area burned and Los Angeles area for December 9th, 2017 at 1800 UTC.

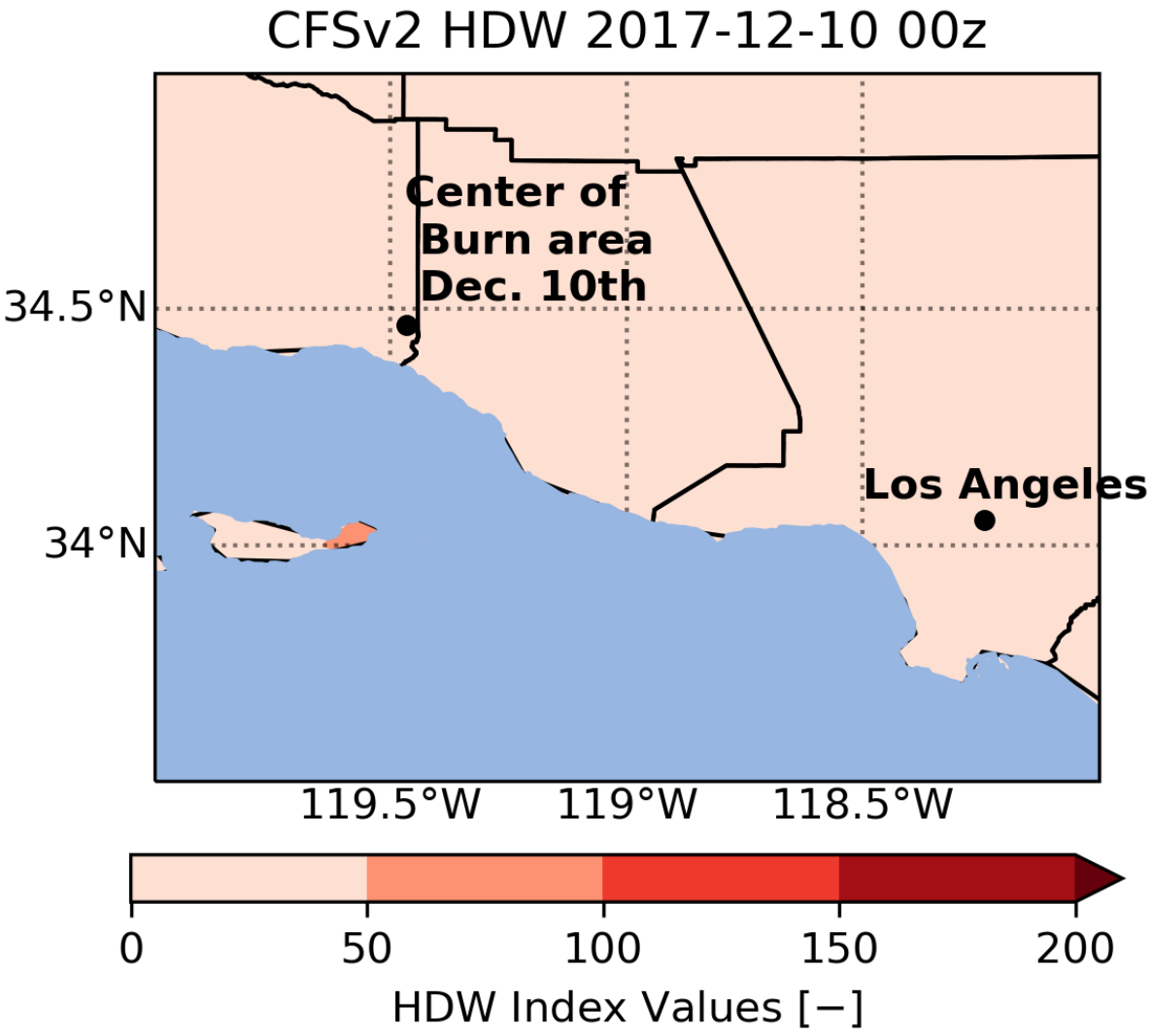

Figure 22: CFSv2 HDW map of the area burned and Los Angeles area for December 10th, 2017 at 0000 UTC.

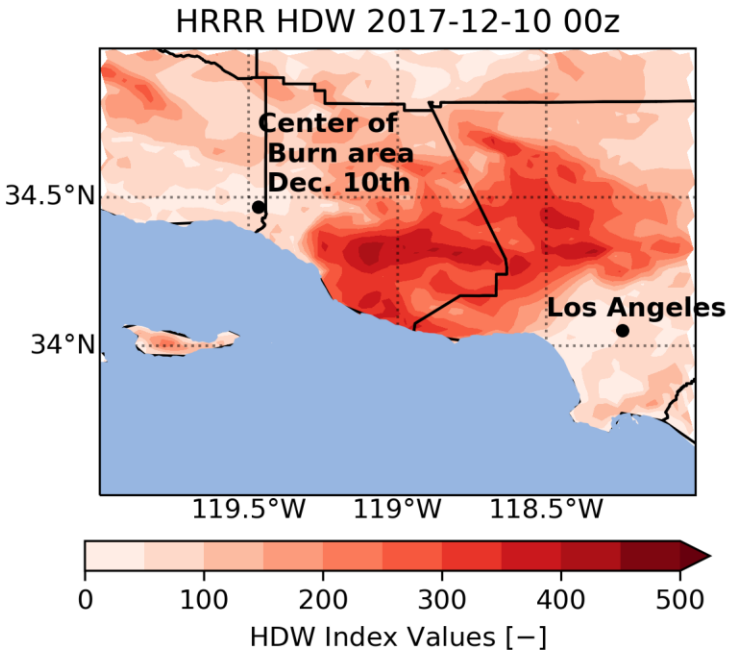

Figure 23: HRRR HDW map of the area burned and Los Angeles area for December 10th, 2017 at 0000UTC.

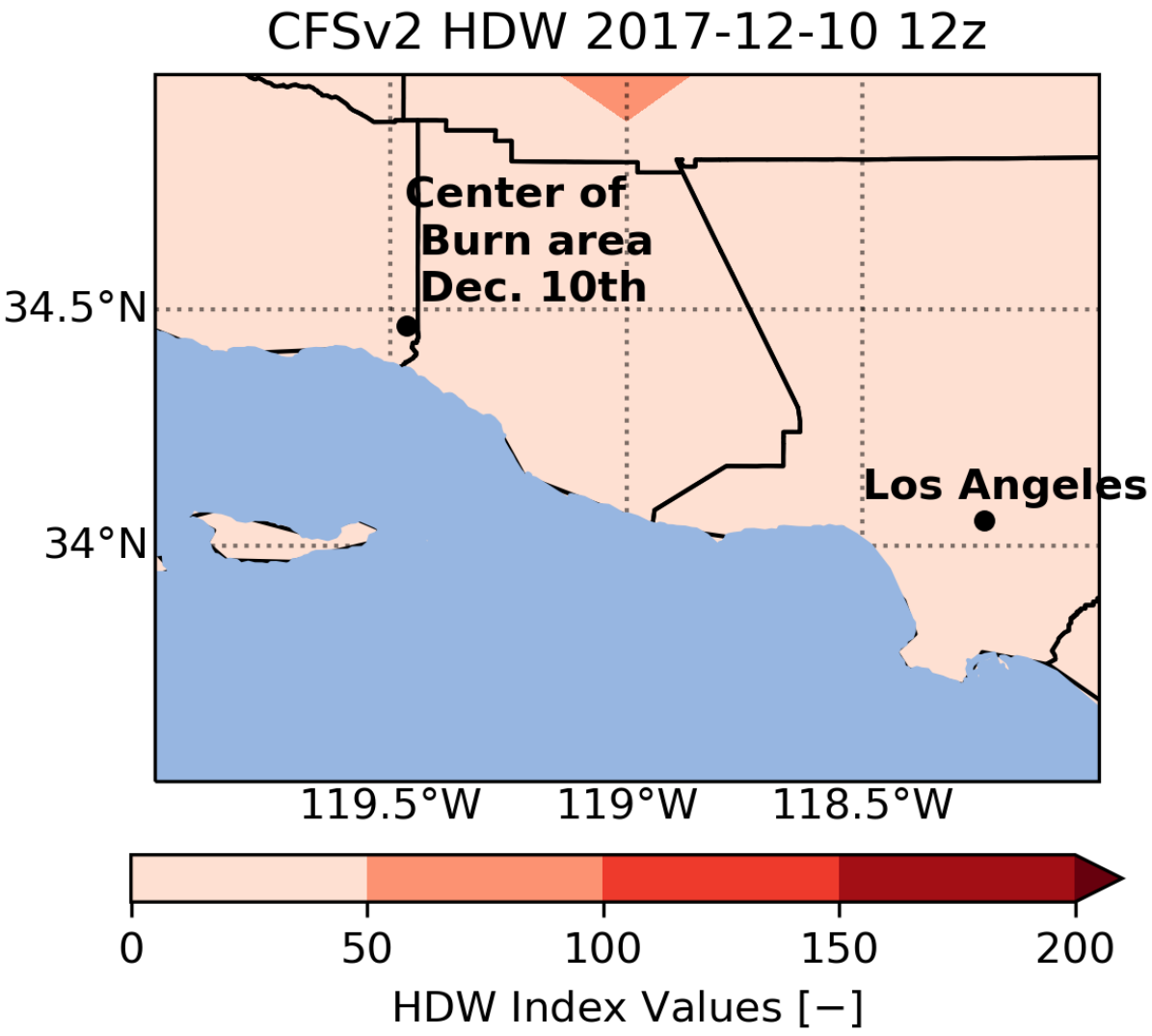

Figure 24: CFSv2 HDW map of the area burned and Los Angeles area for December 10th, 2017 at 1200 UTC.

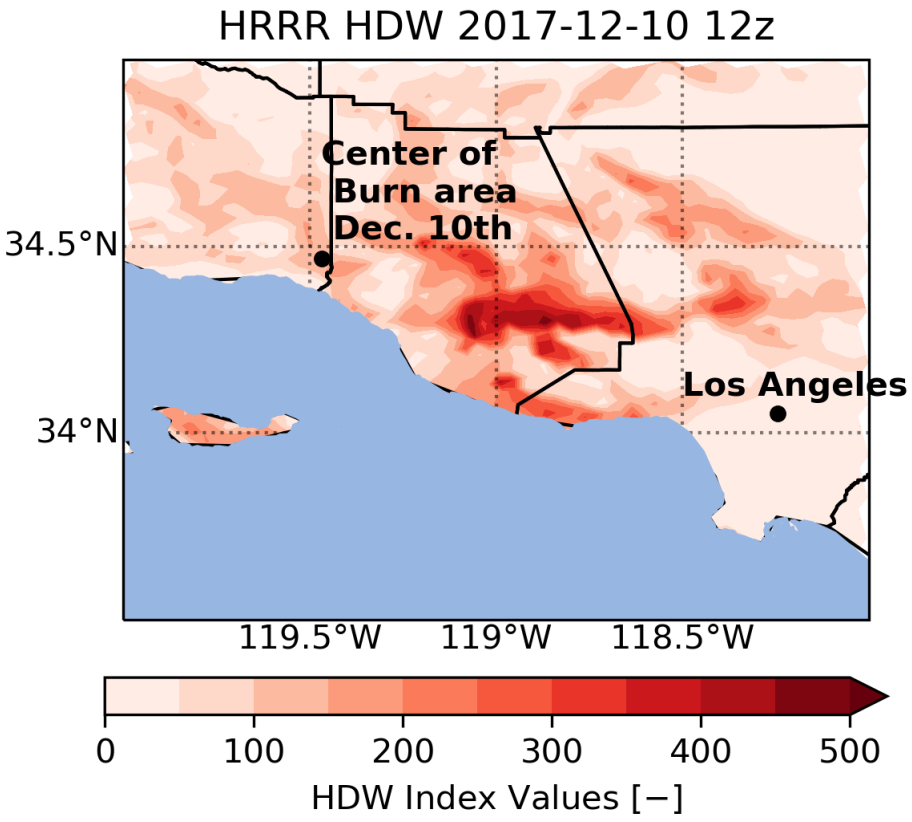

Figure 25: HRRR HDW map of the area burned and Los Angeles area for December 10th, 2017 at 1200 UTC.

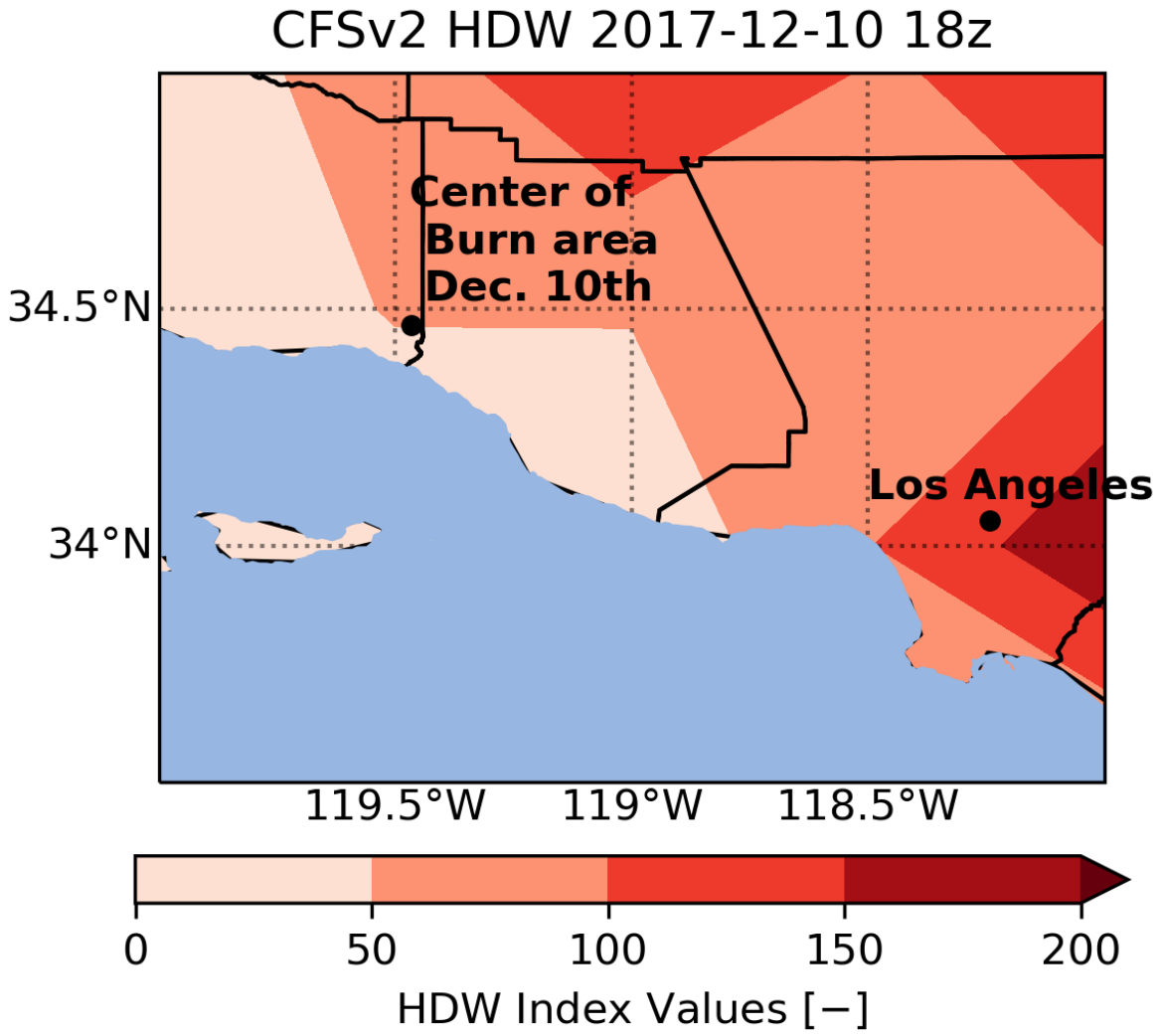

Figure 26: CFSv2 HDW map of the area burned and Los Angeles area for December 10th, 2017 at 1800 UTC.

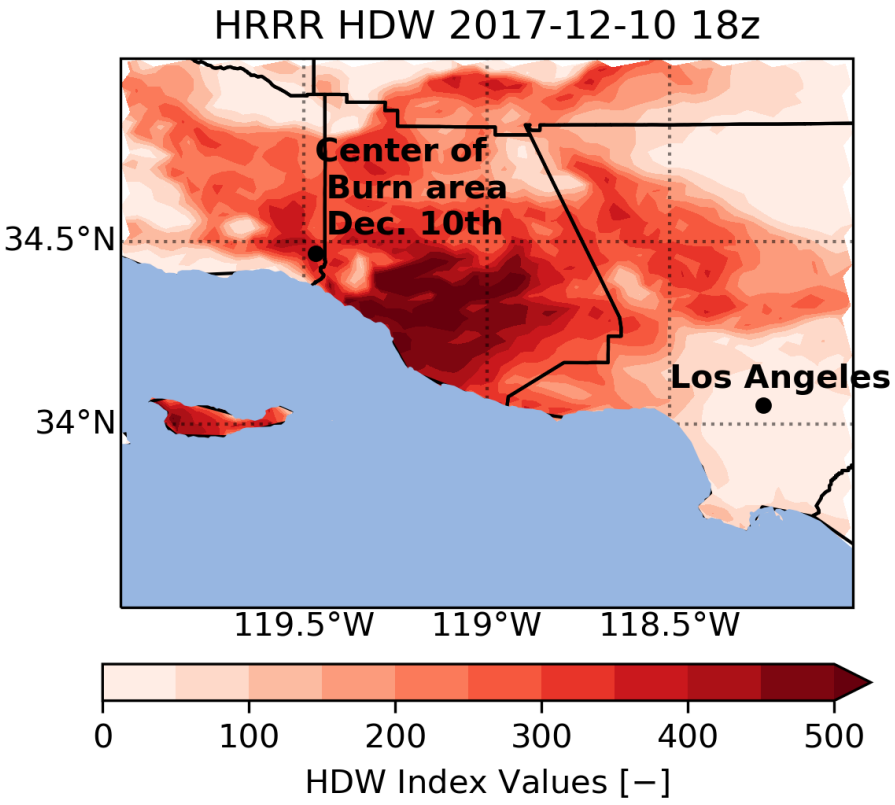

Figure 27: HRRR HDW map of the area burned and Los Angeles area for December 10th, 2017 at 1800 UTC.

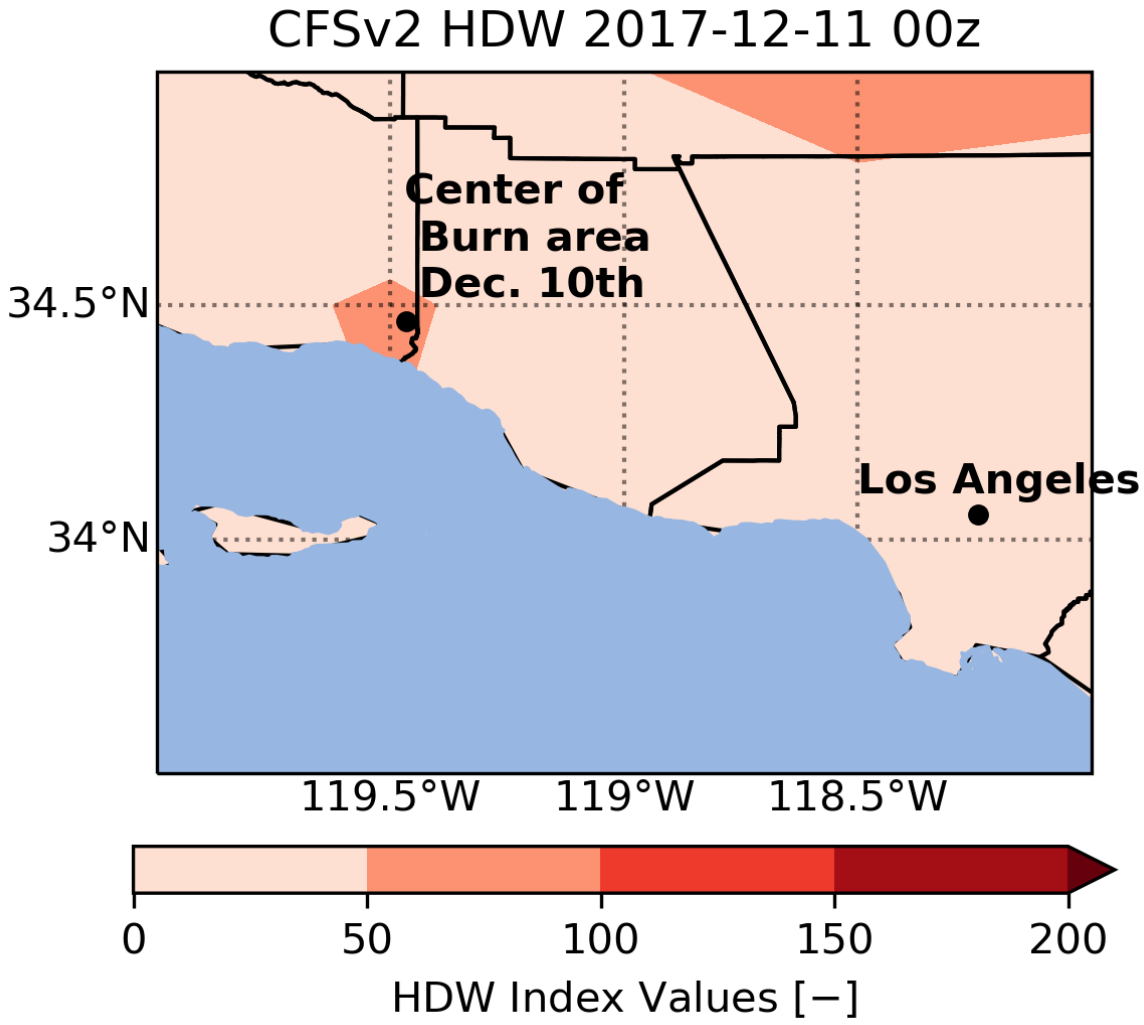

Figure 28: CFSv2 HDW map of the area burned and Los Angeles area for December 11th, 2017 at 0000 UTC.

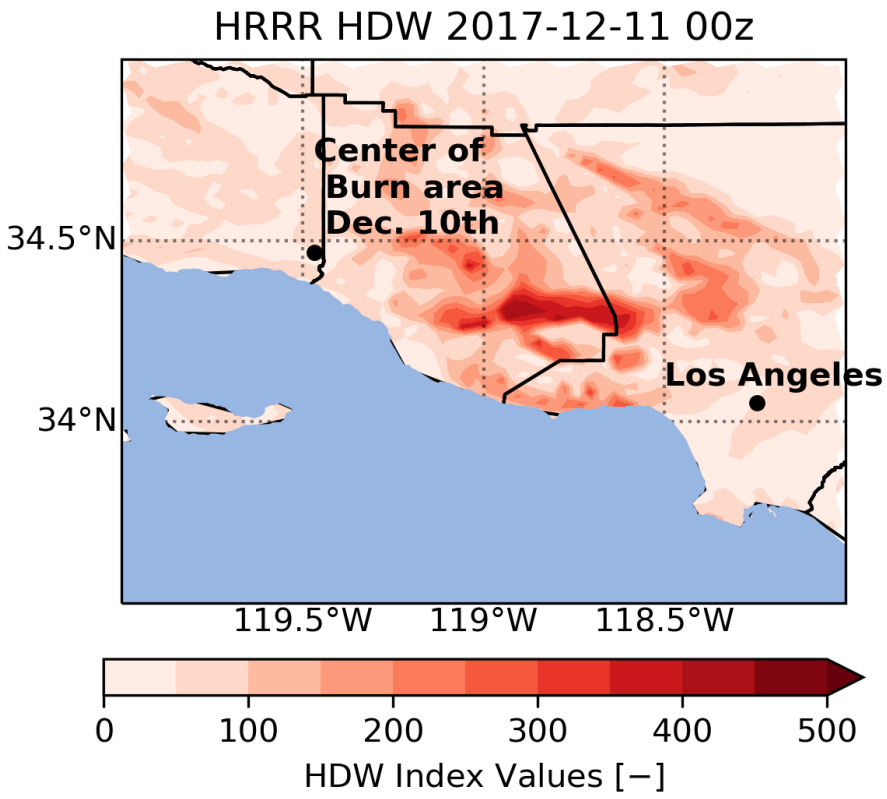

Figure 29: HRRR HDW map of the area burned and Los Angeles area for December 11th, 2017 at 0000 UTC.

Figure 30: The Thomas fire from Faria Beach on December 5th, 2017. Image courtesy of www.noozhawk.com /article/thomas_fire_threatens_ventura_ojai_valley_communities

.

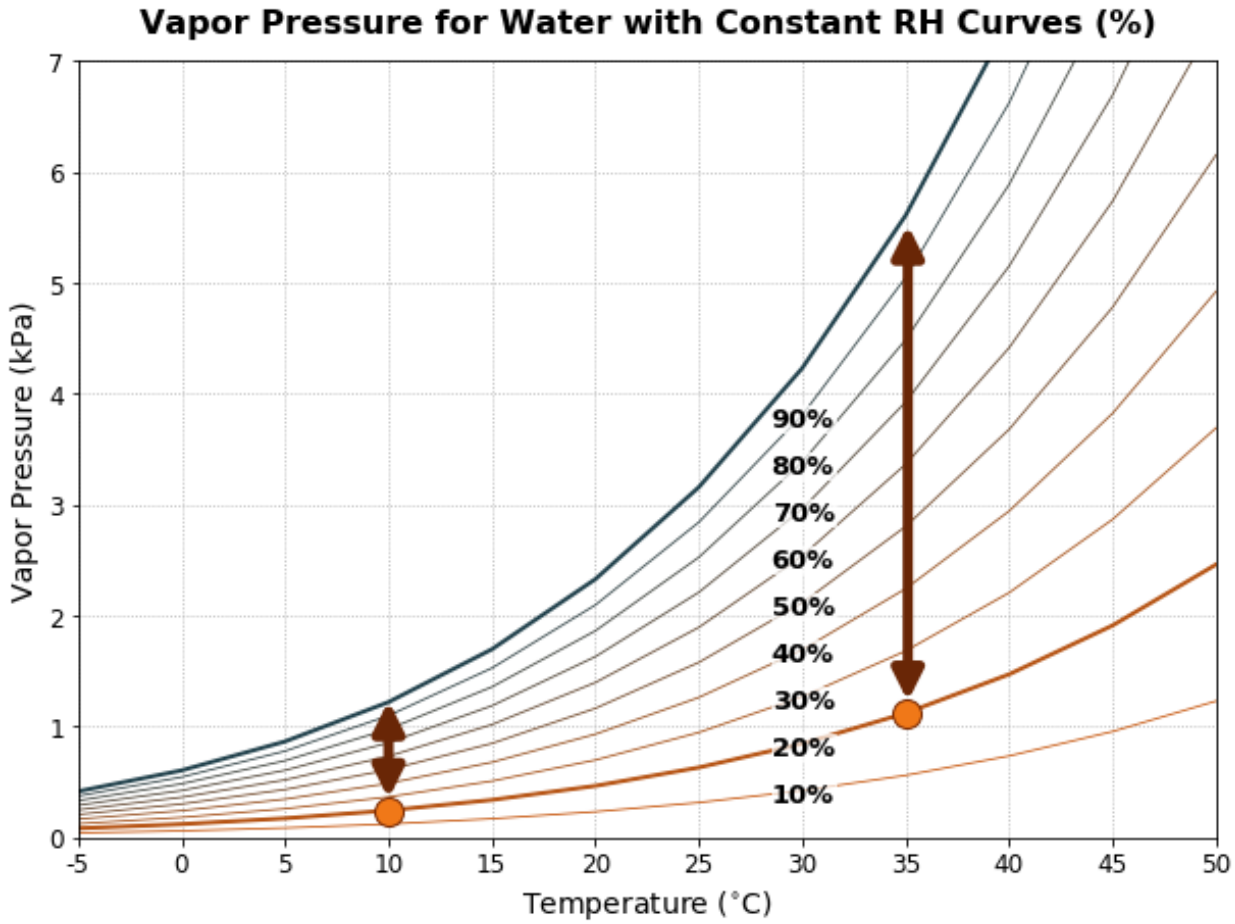

Figure 31: The relationship between temperature and the vapor pressure deficit. Image courtesy of www.hdwindex.org.

Appendix A: METAR Observations

Appendix A1: Oxnard, CA METAR Observations

KOXR 090051Z 29011KT 4SM HZ FU CLR 17/06 A3024 RMK AO2 SLP242 T01670056
KOXR 090151Z 28011KT 5SM HZ FU BKN028 16/02 A3025 RMK AO2 SLP242 T01560017
KOXR 090251Z 33003KT 5SM HZ FU CLR 14/05 A3026 RMK AO2 SLP246 T01440050 53007
KOXR 090351Z 31005KT 4SM HZ FU CLR 13/09 A3026 RMK AO2 SLP246 T01280094
KOXR 090451Z AUTO 00000KT 3SM HZ FU BKN015 13/09 A3026 RMK AO2 SLP247
T01330094
KOXR 090502Z AUTO 29003KT 3SM HZ FU BKN013 13/09 A3026 RMK AO2 T01280089
KOXR 090510Z AUTO 00000KT 2 1/2SM HZ FU BKN011 13/09 A3026 RMK AO2 T01280094
KOXR 090551Z AUTO 05004KT 1 3/4SM HZ FU BKN009 12/07 A3026 RMK AO2 SLP244
T01170067 10189 20111 58000
KOXR 090605Z AUTO 00000KT 1 3/4SM HZ FU SCT009 12/07 A3025 RMK AO2 T01170067
KOXR 090633Z AUTO 08004KT 2SM HZ FU CLR 12/04 A3025 RMK AO2 T01170039
KOXR 090651Z AUTO 05004KT 2 1/2SM HZ FU CLR 13/M02 A3025 RMK AO2 SLP241
T01281017
KOXR 090712Z AUTO 05005KT 3SM HZ FU CLR 14/M04 A3024 RMK AO2 T01391044
KOXR 090751Z AUTO 28005KT 3SM HZ FU CLR 11/M01 A3024 RMK AO2 SLP239 T01061006
402440106
KOXR 090824Z AUTO 33005KT 2SM HZ FU CLR 12/04 A3023 RMK AO2 T01170039
KOXR 090851Z AUTO 33004KT 1 3/4SM HZ FU CLR 12/03 A3023 RMK AO2 SLP236
T01170033 56008
KOXR 090951Z AUTO 00000KT 1 1/4SM HZ FU CLR 11/03 A3023 RMK AO2 SLP234
T01110028
KOXR 091028Z AUTO 34003KT 2 1/2SM HZ FU CLR 14/M02 A3022 RMK AO2 T01391017
KOXR 091049Z AUTO 03008KT 4SM HZ FU CLR 13/M04 A3021 RMK AO2
KOXR 091051Z AUTO 03007KT 4SM HZ FU CLR 14/M05 A3021 RMK AO2 SLP230 T01391050
KOXR 091151Z AUTO 02006KT 5SM HZ FU CLR 15/M08 A3021 RMK AO2 SLP227 T01501078
10161 20106 56007
KOXR 091251Z AUTO 04007KT 6SM HZ FU CLR 16/M08 A3020 RMK AO2 SLP224 T01611078
KOXR 091351Z AUTO 29003KT 6SM HZ FU CLR 13/M06 A3020 RMK AO2 SLP226 T01281056
KOXR 091451Z 29004KT 6SM HZ FU CLR 12/M04 A3021 RMK AO2 SLP230 T01171039
53001
KOXR 091551Z 33003KT 3SM HZ FU CLR 12/M01 A3022 RMK AO2 SLP233 T01171011
KOXR 091651Z 08017KT 10SM FU CLR 24/M09 A3023 RMK AO2 SLP235 T02441094
KOXR 091751Z 07014G24KT 10SM FU CLR 26/M11 A3023 RMK AO2 PK WND 05027/1714
SLP235 T02611106 10261 20100 51007
KOXR 091851Z 06018G29KT 10SM FU CLR 27/M11 A3021 RMK AO2 PK WND 07029/1845
SLP228 T02721111
KOXR 091951Z 07020G26KT 10SM FU CLR 28/M11 A3017 RMK AO2 PK WND 06027/1920
SLP216 T02831111
KOXR 092051Z 07020G30KT 10SM FU CLR 29/M12 A3014 RMK AO2 PK WND 05031/2018
SLP205 T02891122 58030
KOXR 092151Z 07019G27KT 10SM FU CLR 29/M13 A3012 RMK AO2 PK WND 07030/2113
SLP200 T02891128
KOXR 092251Z 08016G28KT 10SM FU CLR 27/M14 A3013 RMK AO2 PK WND 07030/2159
SLP201 T02721139
KOXR 092351Z 08015KT 10SM FU CLR 27/M13 A3013 RMK AO2 SLP201 T02671133 10289
20261 56004
KOXR 100051Z 08012KT 10SM FU CLR 24/M13 A3014 RMK AO2 SLP205 T02441133
KOXR 100151Z 07014KT 10SM FU CLR 24/M13 A3015 RMK AO2 SLP208 T02441133
KOXR 100251Z 07013KT 10SM FU CLR 23/M13 A3016 RMK AO2 SLP213 T02281128 52013
KOXR 100351Z 07010KT 10SM FU CLR 22/M13 A3017 RMK AO2 SLP215 T02221128
KOXR 100451Z AUTO 08011KT 10SM FU CLR 21/M12 A3018 RMK AO2 SLP218 T02111122

KOXR 100551Z AUTO 08014G17KT 10SM FU CLR 21/M13 A3018 RMK AO2 SLP218 T02111128 10267 20200 50005
KOXR 100651Z AUTO 07009KT 10SM FU CLR 21/M13 A3018 RMK AO2 SLP219 T02111128
KOXR 100751Z AUTO 05008KT 10SM FU CLR 22/M12 A3017 RMK AO2 SLP216 T02171122 402890100
KOXR 100851Z AUTO 07013KT 10SM FU CLR 22/M13 A3016 RMK AO2 SLP210 T02221133 58007
KOXR 100951Z AUTO 07014KT 10SM FU CLR 22/M13 A3015 RMK AO2 SLP210 T02221133
KOXR 101051Z AUTO 08012KT 10SM FU CLR 21/M13 A3016 RMK AO2 SLP212 T02111133
KOXR 101151Z AUTO 10008KT 10SM FU CLR 20/M12 A3016 RMK AO2 SLP213 T02001122 10228 20200 53002
KOXR 101251Z AUTO 10008KT 10SM FU CLR 19/M13 A3015 RMK AO2 SLP210 T01891133
KOXR 101351Z AUTO 09010KT 10SM FU CLR 19/M12 A3017 RMK AO2 SLP216 T01891122
KOXR 101451Z 08011KT 10SM FU CLR 20/M13 A3017 RMK AO2 SLP215 T02001133 53002
KOXR 101551Z 09012KT 10SM FU CLR 21/M14 A3018 RMK AO2 SLP217 T02111139
KOXR 101651Z 09011KT 10SM FU CLR 22/M13 A3018 RMK AO2 SLP219 T02221133
KOXR 101751Z 07016KT 10SM FU CLR 26/M13 A3018 RMK AO2 SLP219 T02561133 10256 20183 50004
KOXR 101851Z 07013KT 10SM FU CLR 26/M13 A3017 RMK AO2 SLP217 T02611133
KOXR 101951Z 08014KT 10SM FU CLR 27/M14 A3014 RMK AO2 SLP207 T02721139
KOXR 102051Z 08017G23KT 10SM FU CLR 28/M14 A3012 RMK AO2 SLP197 T02781139 58021
KOXR 102151Z 08016G25KT 10SM FU CLR 28/M14 A3010 RMK AO2 SLP191 T02781144
KOXR 102251Z 07017G24KT 10SM FU CLR 28/M14 A3009 RMK AO2 SLP188 T02781139
KOXR 102351Z 06011KT 10SM FU CLR 27/M14 A3009 RMK AO2 PK WND 08028/2257 SLP187 T02721139 10283 20256 56010
KOXR 110051Z 08011KT 10SM FU CLR 24/M14 A3009 RMK AO2 SLP190 T02441144
KOXR 110151Z 07007KT 10SM FU CLR 23/M15 A3011 RMK AO2 SLP196 T02331150
KOXR 110251Z 06013KT 10SM FU CLR 24/M15 A3012 RMK AO2 SLP197 T02441150 51010
KOXR 110351Z 07010KT 10SM FU CLR 24/M16 A3013 RMK AO2 SLP201 T02391156
KOXR 110451Z AUTO 07009KT 10SM FU CLR 23/M15 A3014 RMK AO2 SLP207 T02331150
KOXR 110551Z AUTO 08009KT 10SM FU CLR 21/M15 A3016 RMK AO2 SLP211 T02111150 10272 20211 51014
KOXR 110651Z AUTO 09007KT 10SM FU CLR 20/M13 A3017 RMK AO2 SLP215 T02001128
KOXR 110751Z AUTO 10005KT 10SM FU CLR 20/M13 A3017 RMK AO2 SLP215 T02001128 402830183
KOXR 110851Z AUTO 09006KT 10SM FU CLR 19/M14 A3016 RMK AO2 SLP213 T01891139 50003
KOXR 110951Z AUTO 07008KT 10SM FU CLR 18/M14 A3016 RMK AO2 SLP212 T01831139
KOXR 111051Z AUTO 08005KT 10SM FU CLR 17/M13 A3016 RMK AO2 SLP213 T01721133
KOXR 111151Z AUTO 10004KT 10SM FU CLR 18/M14 A3015 RMK AO2 SLP209 T01831139 10222 20150 58004
KOXR 111251Z AUTO 07004KT 10SM FU CLR 14/M12 A3015 RMK AO2 SLP209 T01391117
KOXR 111351Z AUTO 06005KT 10SM FU CLR 14/M11 A3016 RMK AO2 SLP213 T01391106
KOXR 111451Z 06005KT 10SM FU CLR 14/M13 A3018 RMK AO2 SLP218 T01441128 53009
KOXR 111551Z 05006KT 10SM FU CLR 17/M10 A3019 RMK AO2 SLP221 T01671100
KOXR 111651Z 07005KT 10SM FU CLR 23/M11 A3020 RMK AO2 SLP226 T02281111
KOXR 111751Z VRB04KT 10SM FU CLR 26/M08 A3022 RMK AO2 SLP232 T02561078 10267 20122 53014
KOXR 111851Z 08012KT 10SM FU CLR 28/M16 A3020 RMK AO2 SLP226 T02831161
KOXR 111951Z 09014KT 10SM FU CLR 29/M17 A3017 RMK AO2 SLP217 T02941167
KOXR 112051Z 20008KT 10SM FU CLR 25/03 A3016 RMK AO2 SLP213 T02500028 56019
KOXR 112151Z 26008KT 5SM HZ FU CLR 22/03 A3017 RMK AO2 SLP214 T02220028
KOXR 112251Z 27006KT 6SM HZ FU CLR 22/03 A3016 RMK AO2 SLP213 T02170028
KOXR 112351Z 27006KT 7SM FU CLR 21/03 A3016 RMK AO2 SLP212 T02110033 10294 20211 58001

Appendix A2: Tonapah, NV (KTPH) METAR Observations

KTPH 090056Z AUTO 32003KT 10SM CLR 08/M14 A3048 RMK AO2 SLP324 T00831144
KTPH 090156Z AUTO 04008KT 10SM CLR 06/M17 A3050 RMK AO2 SLP335 T00611167
KTPH 090256Z AUTO 33010KT 10SM CLR 04/M17 A3052 RMK AO2 SLP345 T00441167
KTPH 090356Z AUTO 01010KT 10SM CLR 03/M16 A3052 RMK AO2 SLP354 T00281161
KTPH 090456Z AUTO 34004KT 10SM CLR 01/M16 A3053 RMK AO2 SLP348 T00061161
KTPH 090556Z AUTO 01016KT 10SM CLR 01/M14 A3053 RMK AO2 SLP345 T00111144
10122 20006 51003
KTPH 090656Z AUTO 34008KT 10SM CLR 00/M15 A3053 RMK AO2 SLP339 T00001150
KTPH 090756Z AUTO 34010KT 10SM CLR M01/M15 A3053 RMK AO2 SLP333 T10061150
KTPH 090856Z AUTO 34010KT 10SM CLR M01/M15 A3053 RMK AO2 SLP330 T10111150
KTPH 090956Z AUTO 35010KT 10SM CLR M01/M16 A3053 RMK AO2 SLP328 T10111156
KTPH 091056Z AUTO 01009KT 10SM CLR M03/M16 A3053 RMK AO2 SLP335 T10331161
KTPH 091156Z AUTO 36007KT 10SM CLR M04/M17 A3052 RMK AO2 SLP337 T10391167
KTPH 091256Z AUTO 36009KT 10SM CLR M04/M17 A3052 RMK AO2 SLP344 T10441167
KTPH 091356Z AUTO 02009KT 10SM CLR M06/M17 A3053 RMK AO2 SLP355 T10561172
KTPH 091456Z AUTO 01009KT 10SM CLR M07/M18 A3055 RMK AO2 SLP366 T10671178
53008
KTPH 091556Z AUTO 04004KT 10SM CLR M05/M18 A3056 RMK AO2 SLP372 T10501178
KTPH 091656Z AUTO 36003KT 10SM CLR M01/M16 A3057 RMK AO2 SLP370 T10061156
KTPH 091756Z AUTO 00000KT 10SM CLR 03/M16 A3057 RMK AO2 SLP361 T00331156
10033 21072 51006
KTPH 091856Z AUTO 00000KT 10SM CLR 07/M15 A3054 RMK AO2 SLP345 T00721150
KTPH 091956Z AUTO 00000KT 10SM CLR 10/M16 A3051 RMK AO2 SLP329 T01001156
KTPH 092056Z AUTO 21004KT 10SM CLR 12/M15 A3048 RMK AO2 SLP316 T01171150
58026
KTPH 092156Z AUTO 20003KT 10SM CLR 13/M14 A3046 RMK AO2 SLP308 T01331144
KTPH 092256Z AUTO 15005KT 10SM CLR 14/M15 A3046 RMK AO2 SLP308 T01441150
KTPH 092356Z AUTO 12005KT 10SM CLR 12/M15 A3046 RMK AO2 SLP317 T01171150
10144 20028 55005
KTPH 100056Z AUTO 01006KT 10SM CLR 07/M16 A3048 RMK AO2 SLP332 T00671161
KTPH 100156Z AUTO 02006KT 10SM CLR 01/M18 A3049 RMK AO2 SLP351 T00111178
KTPH 100256Z AUTO 36008KT 10SM CLR 00/M18 A3051 RMK AO2 SLP361 T00001178
53012
KTPH 100356Z AUTO 36013KT 10SM CLR 01/M19 A3051 RMK AO2 SLP359 T00061194
KTPH 100456Z AUTO 36010KT 10SM CLR 00/M20 A3052 RMK AO2 SLP352 T00001200
KTPH 100556Z AUTO 35007KT 10SM CLR M03/M21 A3053 RMK AO2 SLP356 T10331206
10117 21033 53007
KTPH 100656Z AUTO 36010KT 10SM CLR M03/M21 A3054 RMK AO2 SLP351 T10331206
KTPH 100756Z AUTO 34010KT 10SM CLR M02/M20 A3054 RMK AO2 SLP342 T10221200
401441072
KTPH 100856Z AUTO 36010KT 10SM CLR M03/M21 A3053 RMK AO2 SLP338 T10281206
50000
KTPH 100956Z AUTO 35009KT 10SM CLR M04/M21 A3053 RMK AO2 SLP336 T10391211
KTPH 101056Z AUTO 35009KT 10SM CLR M05/M21 A3053 RMK AO2 SLP336 T10501211
KTPH 101156Z AUTO 36008KT 10SM CLR M06/M22 A3053 RMK AO2 SLP342 T10561217
11017 21061 50000
KTPH 101256Z AUTO 35009KT 10SM CLR M04/M21 A3052 RMK AO2 SLP346 T10391211
KTPH 101356Z AUTO 34009KT 10SM CLR M05/M22 A3053 RMK AO2 SLP362 T10501217
KTPH 101456Z AUTO 36006KT 10SM CLR M07/M22 A3054 RMK AO2 SLP372 T10721222
53002
KTPH 101556Z AUTO 03006KT 10SM CLR M05/M22 A3055 RMK AO2 SLP372 T10501217
KTPH 101656Z AUTO 03004KT 10SM CLR 00/M20 A3056 RMK AO2 SLP368 T00001200
KTPH 101756Z AUTO 00000KT 10SM CLR 04/M19 A3056 RMK AO2 SLP363 T00441189
10044 21083 50006

KTPH 101856Z AUTO 00000KT 10SM CLR 07/M18 A3054 RMK AO2 SLP349 T00721183
KTPH 101956Z AUTO 13003KT 10SM CLR 10/M18 A3050 RMK AO2 SLP330 T01001183
KTPH 102056Z AUTO 00000KT 10SM CLR 12/M19 A3047 RMK AO2 SLP315 T01171189
58026
KTPH 102156Z AUTO 00000KT 10SM CLR 13/M18 A3045 RMK AO2 SLP306 T01331183
KTPH 102256Z AUTO 00000KT 10SM CLR 13/M18 A3044 RMK AO2 SLP305 T01331183
KTPH 102356Z AUTO 15003KT 10SM CLR 13/M19 A3044 RMK AO2 SLP308 T01281189
10139 20044 55008
KTPH 110056Z AUTO 00000KT 10SM CLR 04/M19 A3045 RMK AO2 SLP325 T00441194
KTPH 110156Z AUTO 34007KT 10SM CLR 01/M22 A3046 RMK AO2 SLP340 T00061222
KTPH 110256Z AUTO 36010KT 10SM CLR M01/M23 A3047 RMK AO2 SLP351 T10061228
51009
KTPH 110356Z AUTO 36012KT 10SM CLR M01/M23 A3048 RMK AO2 SLP348 T10111228
KTPH 110456Z AUTO 36011KT 10SM CLR M02/M24 A3048 RMK AO2 SLP342 T10221239
KTPH 110556Z AUTO 35008KT 10SM CLR M03/M23 A3048 RMK AO2 SLP335 T10281233
10128 21033 52004
KTPH 110656Z AUTO 35010KT 10SM CLR M03/M23 A3049 RMK AO2 SLP333 T10331233
KTPH 110756Z AUTO 35012KT 10SM CLR M03/M23 A3049 RMK AO2 SLP326 T10281228
401391083
KTPH 110856Z AUTO 35010KT 10SM CLR M04/M23 A3048 RMK AO2 SLP322 T10391233
58001
KTPH 110956Z AUTO 36007KT 10SM CLR M06/M23 A3049 RMK AO2 SLP328 T10561233
KTPH 111056Z AUTO 36007KT 10SM CLR M07/M24 A3049 RMK AO2 SLP328 T10671244
KTPH 111156Z AUTO 36007KT 10SM CLR M07/M24 A3048 RMK AO2 SLP325 T10671244
11022 21072 50001
KTPH 111256Z AUTO 36010KT 10SM CLR M07/M24 A3048 RMK AO2 SLP343 T10671244
KTPH 111356Z AUTO 36010KT 10SM CLR M06/M24 A3048 RMK AO2 SLP349 T10611244
KTPH 111456Z AUTO 01010KT 10SM CLR M07/M24 A3049 RMK AO2 SLP358 T10721244
53002
KTPH 111556Z AUTO 02005KT 10SM CLR M04/M25 A3051 RMK AO2 SLP359 T10441250
KTPH 111656Z AUTO 01007KT 10SM CLR 02/M24 A3051 RMK AO2 SLP350 T00171239
KTPH 111756Z AUTO 18004KT 10SM CLR 02/M22 A3051 RMK AO2 SLP351 T00221222
10039 21083 51007
KTPH 111856Z AUTO 14003KT 10SM CLR 06/M21 A3050 RMK AO2 SLP339 T00611211
KTPH 111956Z AUTO 00000KT 10SM CLR 07/M21 A3048 RMK AO2 SLP328 T00721206
KTPH 112056Z AUTO VRB03KT 10SM CLR 10/M19 A3046 RMK AO2 SLP316 T01001189
58017
KTPH 112156Z AUTO VRB03KT 10SM CLR 12/M18 A3044 RMK AO2 SLP310 T01221178
KTPH 112256Z AUTO 18003KT 10SM CLR 12/M18 A3044 RMK AO2 SLP311 T01221183
KTPH 112356Z AUTO 11005KT 10SM CLR 10/M19 A3044 RMK AO2 SLP317 T01001189
10128 20022 55004

Appendix A3: Los Angeles, CA (KLAX) METAR Observations

KLAX 090053Z 26010KT 3SM HZ SCT000 BKN100 BKN150 19/05 A3023 RMK AO2 SLP236 FU SCT000 T01890050
KLAX 090153Z 24006KT 4SM HZ SCT000 BKN100 BKN120 18/07 A3023 RMK AO2 SLP237 FU SCT000 T01780067
KLAX 090253Z 00000KT 4SM HZ FEW000 SCT100 17/08 A3023 RMK AO2 SLP236 FU FEW000 T01670083 50000
KLAX 090353Z 10005KT 4SM HZ FEW000 FEW100 17/07 A3023 RMK AO2 SLP237 FU FEW000 T01670072
KLAX 090453Z 12004KT 4SM HZ FEW000 17/06 A3024 RMK AO2 SLP239 FU FEW000 T01670061
KLAX 090553Z 00000KT 9SM FEW000 SCT200 17/01 A3025 RMK AO2 SLP241 VIS S-W 3 FU FEW000 T01670011 10228 20161 53007
KLAX 090653Z VRB03KT 10SM FEW001 SCT200 17/M03 A3024 RMK AO2 SLP238 FU FEW001 T01671028
KLAX 090753Z VRB03KT 10SM FEW001 SCT200 18/M05 A3023 RMK AO2 SLP233 FU FEW001 T01831050 402560111
KLAX 090853Z 11003KT 10SM FEW001 SCT200 15/M04 A3022 RMK AO2 SLP231 FU FEW001 T01501044 58009
KLAX 090953Z 00000KT 10SM FEW001 BKN200 14/M04 A3022 RMK AO2 SLP230 FU FEW001 T01441039
KLAX 091053Z 10005KT 10SM BKN200 14/M04 A3021 RMK AO2 SLP229 T01391039
KLAX 091153Z 00000KT 10SM BKN200 13/M02 A3021 RMK AO2 SLP227 T01281022 10194 20111 58005
KLAX 091253Z 07004KT 10SM BKN200 13/M06 A3020 RMK AO2 SLP225 T01331056
KLAX 091353Z 12003KT 10SM BKN200 14/M06 A3021 RMK AO2 SLP227 T01391061
KLAX 091453Z 06004KT 10SM BKN200 16/M07 A3022 RMK AO2 SLP230 T01561067 53003
KLAX 091553Z 08003KT 10SM FEW050 BKN200 17/M07 A3022 RMK AO2 SLP233 T01671067
KLAX 091653Z VRB03KT 10SM FEW050 BKN200 22/M08 A3023 RMK AO2 SLP236 T02221078
KLAX 091753Z 07004KT 10SM FEW015 FEW050 BKN200 24/M08 A3023 RMK AO2 SLP235 FU FEW015 T02391083 10239 20122 51007
KLAX 091853Z 05004KT 10SM FEW050 BKN200 26/M09 A3021 RMK AO2 SLP228 T02611089
KLAX 091953Z 13005KT 10SM FEW050 BKN200 27/M10 A3017 RMK AO2 SLP217 T02721100
KLAX 092053Z VRB04KT 10SM FEW050 BKN200 29/M12 A3014 RMK AO2 SLP205 T02891117 58029
KLAX 092153Z 13004KT 10SM FEW050 BKN200 29/M13 A3012 RMK AO2 SLP199 T02941133
KLAX 092253Z 29008KT 10SM FEW045 FEW100 BKN200 28/M06 A3011 RMK AO2 SLP196 T02831061
KLAX 092353Z 29006KT 10SM FEW022 FEW080 BKN200 27/M08 A3011 RMK AO2 SLP198 FU FEW022 T02671083 10300 20239 55008
KLAX 100053Z VRB03KT 10SM FEW022 FEW080 BKN200 25/M08 A3012 RMK AO2 SLP201 FU FEW022 T02501083
KLAX 100153Z VRB03KT 10SM SCT200 24/M06 A3014 RMK AO2 SLP205 T02391061
KLAX 100253Z 00000KT 10SM SCT200 23/M06 A3015 RMK AO2 SLP210 T02331056 53013
KLAX 100353Z 00000KT 10SM SCT200 22/M11 A3016 RMK AO2 SLP212 T02171106
KLAX 100453Z 00000KT 10SM SCT200 22/M11 A3017 RMK AO2 SLP214 T02221106
KLAX 100553Z 05003KT 10SM SCT200 18/M07 A3017 RMK AO2 SLP215 T01831067 10267 20183 51006
KLAX 100653Z 00000KT 10SM BKN200 19/M07 A3018 RMK AO2 SLP216 T01891067
KLAX 100753Z 12003KT 10SM BKN200 16/M06 A3017 RMK AO2 SLP212 T01611056 403000111
KLAX 100853Z VRB03KT 10SM BKN200 17/M07 A3016 RMK AO2 SLP210 T01671067 58004
KLAX 100953Z 06004KT 10SM SCT200 17/M08 A3016 RMK AO2 SLP210 T01721078
KLAX 101053Z 02003KT 10SM FEW200 16/M07 A3016 RMK AO2 SLP211 T01611072

KLAX 101153Z 35003KT 10SM CLR 14/M07 A3016 RMK AO2 SLP207 T01441067 10206 20128 58003
KLAX 101253Z 00000KT 10SM FEW200 13/M07 A3016 RMK AO2 SLP208 T01281067
KLAX 101353Z 09005KT 10SM FEW150 SCT200 12/M05 A3017 RMK AO2 SLP214 T01171050
KLAX 101453Z 00000KT 10SM FEW150 SCT200 BKN300 14/M08 A3017 RMK AO2 SLP214 T01391078 53006
KLAX 101553Z 06003KT 10SM FEW055 FEW180 SCT230 BKN300 17/M10 A3018 RMK AO2 SLP219 FU FEW055 T01721100
KLAX 101653Z 05004KT 10SM FEW055 FEW180 SCT230 BKN300 21/M11 A3019 RMK AO2 SLP219 FU FEW055 T02061106
KLAX 101753Z 00000KT 10SM FEW060 FEW180 BKN230 BKN300 21/M08 A3018 RMK AO2 SLP219 FU FEW060 T02111083 10211 20106 50005
KLAX 101853Z 00000KT 10SM FEW060 FEW180 BKN230 BKN300 24/M09 A3016 RMK AO2 SLP211 FU FEW060 T02441089
KLAX 101953Z 32004KT 10SM FEW060 BKN230 BKN300 28/M08 A3013 RMK AO2 SLP203 FU FEW060 T02781083
KLAX 102053Z 34004KT 10SM FEW055 FEW110 SCT230 BKN300 29/M09 A3010 RMK AO2 SLP193 FU FEW055 FU FEW110 T02891094 58025
KLAX 102153Z 00000KT 10SM FEW055 FEW110 SCT230 BKN300 28/M11 A3008 RMK AO2 SLP186 FU FEW055 FU FEW110 T02831106
KLAX 102253Z 32006KT 10SM FEW055 OVC200 28/M12 A3008 RMK AO2 SLP184 FU FEW055 T02831117
KLAX 102353Z 32005KT 10SM OVC200 28/M09 A3008 RMK AO2 SLP183 T02781094 10294 20211 56009
KLAX 110053Z 35006KT 10SM FEW055 BKN200 26/M10 A3008 RMK AO2 SLP185 FU FEW055 T02611100
KLAX 110153Z 03003KT 10SM OVC200 24/M10 A3010 RMK AO2 SLP193 T02391100
KLAX 110253Z 00000KT 10SM OVC200 23/M11 A3012 RMK AO2 SLP199 T02331111 53014
KLAX 110353Z 00000KT 10SM OVC200 22/M09 A3013 RMK AO2 SLP203 T02221089
KLAX 110453Z 00000KT 10SM BKN200 22/M09 A3015 RMK AO2 SLP206 T02171089
KLAX 110553Z 04007KT 10SM SCT200 22/M08 A3016 RMK AO2 SLP211 T02171078 10278 20211 53014
KLAX 110653Z 00000KT 10SM SCT200 BKN280 20/M08 A3017 RMK AO2 SLP213 T02001078
KLAX 110753Z 00000KT 10SM SCT200 BKN280 21/M10 A3016 RMK AO2 SLP210 T02111100 402940106
KLAX 110853Z 00000KT 10SM FEW200 BKN280 18/M08 A3016 RMK AO2 SLP210 T01781078 58001
KLAX 110953Z 06003KT 10SM FEW200 BKN280 17/M08 A3017 RMK AO2 SLP212 T01721078
KLAX 111053Z 04005KT 10SM FEW200 BKN280 17/M08 A3016 RMK AO2 SLP209 T01721078
KLAX 111153Z 06005KT 10SM FEW200 BKN280 16/M09 A3015 RMK AO2 SLP205 T01611089 10228 20156 58005
KLAX 111253Z 00000KT 10SM FEW200 SCT280 17/M11 A3015 RMK AO2 SLP206 T01721106
KLAX 111353Z VRB03KT 10SM SCT180 BKN250 15/M09 A3016 RMK AO2 SLP210 T01501094
KLAX 111453Z 05005KT 10SM SCT090 SCT180 BKN250 17/M11 A3017 RMK AO2 SLP215 T01671106 53009
KLAX 111553Z 09005KT 10SM SCT090 SCT180 BKN250 16/M09 A3020 RMK AO2 SLP223 T01611089
KLAX 111653Z VRB04KT 10SM FEW100 SCT180 BKN250 22/M11 A3021 RMK AO2 SLP227 T02171106
KLAX 111753Z 06004KT 10SM FEW100 FEW180 BKN250 24/M10 A3022 RMK AO2 SLP232 T02391100 10239 20139 51017
KLAX 111853Z VRB04KT 10SM FEW100 SCT160 SCT200 27/M12 A3021 RMK AO2 SLP228 T02671117
KLAX 111953Z 00000KT 10SM FEW100 SCT140 BKN180 28/M13 A3018 RMK AO2 SLP219 T02781128
KLAX 112053Z VRB03KT 10SM FEW080 FEW110 SCT150 BKN200 28/M14 A3016 RMK AO2 SLP212 T02831139 58019

KLAX 112153Z 27006KT 10SM FEW005 FEW080 SCT160 BKN220 24/M05 A3016 RMK AO2 SLP210 FU FEW005 T02441050
KLAX 112253Z 29010KT 10SM FEW200 SCT250 24/M09 A3016 RMK AO2 SLP211 T02391089
KLAX 112353Z 29009KT 10SM SCT200 SCT250 22/M06 A3016 RMK AO2 SLP212 T02221056 10283 20222 56002

Appendix B: Selected Sea Condition Measurements for Santa Monica Basin Buoy

From the National Buoy Data Center

https://www.ndbc.noaa.gov/view_text_file.php?filename=46025h2017.txt.gz&dir=data/historical/stdmet/

Accessed 11/30/2020

```
#YY  MM DD hh mm WDIR WSPD GST  WVHT   DPD   APD MWD   PRES  ATMP  WTMP  DEWP
VIS  TIDE

2017 12 09 12 00   4  0.5  0.8 99.00 99.00 99.00 999 1022.1 999.0  15.5 999.0
99.0 99.00

2017 12 09 18 00  30  1.7  2.2 99.00 99.00 99.00 999 1023.2 999.0  16.2 999.0
99.0 99.00

2017 12 10 00 00 282  2.6  3.0 99.00 99.00 99.00 999 1019.7 999.0  16.2 999.0
99.0 99.00

2017 12 10 06 00  63  3.3  4.0 99.00 99.00 99.00 999 1021.1 999.0  15.5 999.0
99.0 99.00

2017 12 10 12 00  55  2.6  3.2 99.00 99.00 99.00 999 1020.2 999.0  16.5 999.0
99.0 99.00

2017 12 10 18 00  62  1.6  2.3 99.00 99.00 99.00 999 1021.3 999.0  15.5 999.0
99.0 99.00

2017 12 11 00 10 269  2.5  3.0 99.00 99.00 99.00 999 1018.1 999.0  15.7 999.0
99.0 99.00

2017 12 11 06 00  55  3.3  4.0 99.00 99.00 99.00 999 1020.4 999.0  15.6 999.0
99.0 99.00

2017 12 11 12 00  58  1.4  1.8 99.00 99.00 99.00 999 1020.2 999.0  16.0 999.0
99.0 99.00

2017 12 11 18 00 245  1.1  1.7 99.00 99.00 99.00 999 1022.9 999.0  15.9 999.0
99.0 99.00

2017 12 12 00 00 335  2.6  3.6 99.00 99.00 99.00 999 1021.0 999.0  16.3 999.0
99.0 99.00
```

Works Cited

Abatzoglou, J. T., R. Barbero, and N. J. Nauslar, 2013: Diagnosing Santa Ana Winds in Southern California with Synoptic-Scale Analysis. *Wea. Forecasting*, **28**, 704–710, https://doi.org/10.1175/WAF-D-13-00002.1.

Arizona Department of Forestry and Fire Management, 2013. *Yarnell Hill Fire June 30th, 2013 Serious Accident Investigation Report*. Phoenix, AZ: Arizona Department of Forestry and Fire Management, p.120.

Benjamin et al. 2016, A North American Hourly Assimilation and Model Forecast Cycle: The Rapid Refresh. *Mon. Wea. Rev.*, **144**, 1669-1694.

Brewer, M. C., C. F. Mass, and B. E. Potter, 2012: The West Coast Thermal Trough: Climatology and Synoptic Evolution. *Mon. Wea. Rev.*, **140**, 3820–3843, https://doi.org/10.1175/MWR-D-12-00078.1.

Byram, George M. 1954. Atmospheric conditions related to blowup fires. Station Paper SE-SP-35. Asheville, NC: USDA-Forest Service. Southeastern Forest Experiment Station. 36 pp.

Hoover, K., Hanson, L. A., 2021. *Wildfire Statistics*, Congressional Research Service, p.3

Hoerling, M. P., M. Dettinger, K. Wolter, J. Lukas, J. Eischeid, R. Nemani, B. Liebmann, and K. E. Kunkel. 2013. "Present Weather and Climate: Evolving Conditions." In Assessment of Climate Change in the Southwest United States: A Report Prepared for the National Climate Assessment, edited by G. Garfin, A. Jardine, R. Merideth, M. Black, and S. LeRoy, 74–100. A report by the Southwest Climate Alliance. Washington, DC: Island Press.

McDonald, J.M., Srock, A.F., and Charney, J.J., 2018: Development and application of a Hot-Dry-Windy Index (HDW) climatology. *Atmosphere*, **9**, 285. doi: https://doi.org/10.3390/atmos9070285

Raphael, M. N., 2003: The Santa Ana Winds of California. *Earth Interact.*, **7**, 1–13, https://doi.org/10.1175/1087-3562(2003)007<0001:TSAWOC>2.0.CO;2.

Rolinski, T., S. B. Capps, R. G. Fovell, Y. Cao, B. J. D'Agostino, and S. Vanderburg, 2016: The Santa Ana Wildfire Threat Index: Methodology and Operational Implementation. *Wea. Forecasting*, **31**, 1881–1897, https://doi.org/10.1175/WAF-D-15-0141.1.

Rolinski, T., S. B. Capps, and W. Zhuang, 2019: Santa Ana Winds: A Descriptive Climatology. *Wea. Forecasting*, **34**, 257–275, https://doi.org/10.1175/WAF-D-18-0160.1.

Saha, Suranjana and Coauthors, 2014: The NCEP Climate Forecast System Version 2 *Journal of Climate J. Climate*, **27**, 2185–2208. doi: http://dx.doi.org/10.1175/JCLI-D-12-00823.1

Small, I. J., 1995: Santa Ana Winds and the fire outbreak of fall 1993. NOAA Tech. Memo. NWS WR-230, 48 pp.

Srock, A.F., Charney, J.J., Potter, B.E., and Goodrick, S.L., 2018: The Hot-Dry-Windy Index: A new fire weather index. *Atmosphere*, **9**, 279. doi: https://doi.org/10.3390/atmos9070279